

SN 2013ab : A normal type IIP supernova in NGC 5669

Subhash Bose^{1,2*}, Stefano Valenti^{3,4}, Kuntal Misra¹, Maria Letizia Pumo^{5,6,7}, Luca Zampieri⁵, David Sand⁸, Brijesh Kumar¹, Andrea Pastorello⁵, Firoza Sutaria⁹, Thomas J. Maccarone⁸, Brajesh Kumar^{1,10}, M. L. Graham¹¹, D. Andrew Howell^{3,4}, Paolo Ochner⁵, H. C. Chandola², Shashi B. Pandey¹

¹*Aryabhatta Research Institute of Observational Sciences, Manora Peak, Nainital - 263002, India.*

²*Centre of Advance Study, Department of Physics, Kumaun University, Nainital - 263001, India.*

³*Las Cumbres Observatory Global Telescope Network, 6740 Cortona Dr., Suite 102, Goleta, CA 93117, USA*

⁴*Department of Physics, University of California, Santa Barbara, Broida Hall, Mail Code 9530, Santa Barbara, CA 93106-9530, USA*

⁵*INAF, Osservatorio Astronomico di Padova, 35122 Padova, Italy*

⁶*Università di Catania, Dip. di Fisica e Astronomia (Sez. astrofisica), via S. Sofia 78, 95123 Catania, Italy*

⁷*INAF-Osservatorio Astronomico di Palermo, Piazza del Parlamento 1, 90134 Palermo, Italy*

⁸*Physics Department, Texas Tech University, Lubbock, TX 79409, USA*

⁹*Indian Institute of Astrophysics, Block-II, Koramangala, Bangalore - 560034, India.*

¹⁰*Institut d’Astrophysique et de Géophysique, Université de Liège, Allée du 6 Août 17, Bât B5c, 4000 Liège, Belgium*

¹¹*Department of Astronomy, University of California, Berkeley, CA 94720-3411 USA*

Accepted.....; Received

ABSTRACT

We present densely-sampled ultraviolet/optical photometric and low-resolution optical spectroscopic observations of the type IIP supernova 2013ab in the nearby (~ 24 Mpc) galaxy NGC 5669, from 2 to 190d after explosion. Continuous photometric observations, with the cadence of typically a day to one week, were acquired with the 1-2m class telescopes in the LCOGT network, ARIES telescopes in India and various other telescopes around the globe. The light curve and spectra suggest that the SN is a normal type IIP event with a plateau duration of ~ 80 days with mid plateau absolute visual magnitude of -16.7, although with a steeper decline during the plateau (0.92 mag 100 d⁻¹ in *V* band) relative to other archetypal SNe of similar brightness. The velocity profile of SN 2013ab shows striking resemblance with those of SNe 1999em and 2012aw. Following the Rabinak & Waxman (2011) prescription, the initial temperature evolution of the SN emission allows us to estimate the progenitor radius to be ~ 800 R_⊙, indicating that the SN originated from a red supergiant star. The distance to the SN host galaxy is estimated to be 24.3 Mpc from expanding photosphere method (EPM). From our observations, we estimate that 0.064 M_⊙ of ⁵⁶Ni was synthesized in the explosion. General relativistic, radiation hydrodynamical modeling of the SN infers an explosion energy of 0.35×10^{51} erg, a progenitor mass (at the time of explosion) of ~ 9 M_⊙ and an initial radius of ~ 600 R_⊙.

Key words: supernovae: general – supernovae: individual: SN 2013ab – galaxies: individual: NGC 5669

1 INTRODUCTION

Type IIP supernovae (SNe) are a sub-class of Core-Collapse SNe (CCSNe) whose progenitors had retained substantial amount of hydrogen before they exploded as SNe. These SNe exhibit nearly constant brightness in their light curve for a few months after explosion, known as plateau phase. This is explained as a combined effect of expanding ejecta and

receding recombination layer of hydrogen due to adiabatic cooling of the envelope (e.g. Kasen & Woosley 2009). After reaching the end of plateau phase, a type IIP SN light curve shows a very steep decline and then finally settles on to a relatively slowly declining phase labelled as the radioactive tail. This stage, also called the nebular phase, is powered by the radiation originating from the radioactive decay of ⁵⁶Co to ⁵⁶Fe (Arnett 1980) which in turn depends upon the amount ⁵⁶Ni synthesized in the explosion.

* e-mail: email@subhashbose.com, bose@aries.res.in

Type IIP SNe are also proven candidates for distance

Table 1. Properties of the SN 2013ab and its host galaxy NGC 5669.

Parameters	Value	Ref. ^a
NGC 5669:		
Type	Sb	2
RA (J2000)	$\alpha = 14^{\text{h}}32^{\text{m}}43\overset{\text{s}}{.}8$	2
DEC (J2000)	$\delta = 09^{\circ}53'28\overset{\text{.}}{''}8$	2
Abs. Magnitude	$M_B = -19.28$ mag	2
Distance	$D = 24.0 \pm 0.9$ Mpc	1
Distance modulus	$\mu = 31.90 \pm 0.08$ mag	
Heliocentric Velocity	$cz_{\text{helio}} = 1374 \pm 2$ km s ⁻¹	2
SN 2013ab:		
RA (J2000)	$\alpha = 14^{\text{h}}32^{\text{m}}44\overset{\text{s}}{.}49$	3
DEC (J2000)	$\delta = 09^{\circ}53'12\overset{\text{.}}{''}3$	
Galactocentric Location	7''.5 E, 18''.1 S	
Time of explosion	$t_0 = 16.5$ February 2013 (UT) (JD 2456340.0 \pm 1.0) day	1
Total reddening	$E(B-V) = 0.044 \pm 0.066$ mag	1

(1) This paper; (2) HyperLEDA - <http://leda.univ-lyon1.fr> (Makarov et al. 2014); (3) Zheng et al. (2013)

estimation at extragalactic scales. Hamuy (2001) explored the potential of these SNe as standardizable candles. The expanding photosphere method (EPM) (Kirshner & Kwan 1974) for estimating distances has also been applied extensively. Significant contribution has been made to improve and implement EPM by several authors, viz. Hamuy et al. (2001); Dessart & Hillier (2005a); Jones et al. (2009); Bose & Kumar (2014). EPM requires an extensive set of photometric and spectroscopic data of SNe.

According to our current understanding of stellar evolution, type IIP SNe originate from red supergiant (RSG) stars having initial masses of $9-25 M_{\odot}$, with an upper mass limit of $\sim 32 M_{\odot}$, for solar metallicity stars (e.g. Heger et al. 2003). Recent studies also identified Super-AGB stars as potential progenitors of some SNe IIP (see e.g. Pumo et al. 2009, and references therein). However there is a limited number of nearby SNe where high resolution pre-SN *HST* images are available. The estimated range of masses for these progenitors from direct observations lies within $9-17 M_{\odot}$ (Smartt et al. 2009). On the other hand, hydrodynamical modeling of a handful of well-studied SN light curves suggests that their progenitor masses are within $15-25 M_{\odot}$ (Utrobin & Chugai 2009; Bersten et al. 2011).

The cosmological importance of type IIP SNe and the ambiguity in the present understanding of their evolution and physical mechanisms are key motivations to study individual events with a range of properties. One of the best observed recent type IIP event is SN 2013ab

SN 2013ab was discovered on February 17.5 UTC, 2013 by Blanchard et al. (2013) in the galaxy NGC 5669 (~ 25 Mpc) (see Fig. 1) at $R \sim 17.6$ mag. The last non-detection was reported on February 15 (Zheng et al. 2013) to a limiting magnitude $R \sim 18.5$. We therefore adopt February 16.5, 2013 (JD=2456340.0 \pm 1.0 days) as the time of explosion.

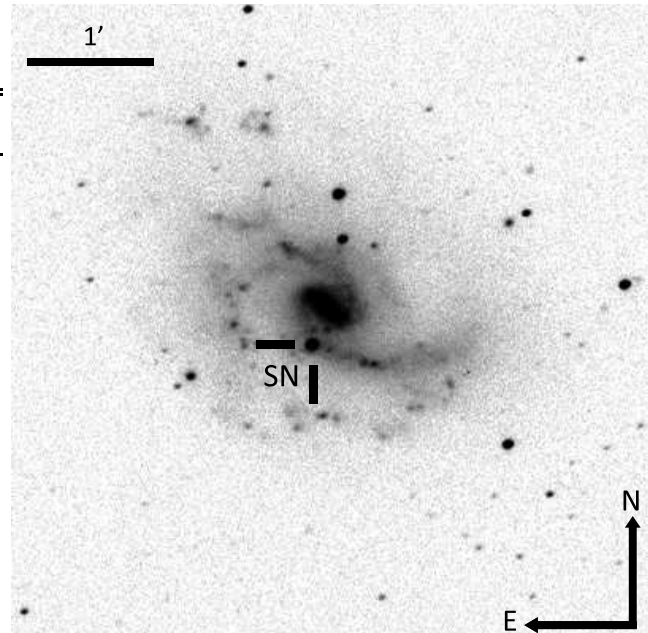


Figure 1. SN 2013ab in NGC 5669. The V -band image taken from 104-cm ST covering a subsection of about $5'.1 \times 5'.1$ is shown.

(0d phase) throughout the paper. Some basic parameters of SN 2013ab and its host galaxy are listed in Table 1.

In this work, we present results from optical photometric (*UBVRI* and *gri*) follow-up observations of SN 2013ab at 136 phases (from 3 to 190d), *Swift* UVOT observations at 25 epochs (from 4 to 103d) and low-resolution optical spectroscopic observations at 25 phases (from 2 to 184d). The paper is organized as follows. The §2 provides details of the photometric and spectroscopic observations. Determination of reddening and extinction is described in §3. In §4, we study the light and colour curves, derive bolometric light curves whose tail luminosities are used to estimate the ^{56}Ni mass. In §5, we study the spectral evolution, present SYNOW modelling and derive line velocities. Application of EPM and estimate of distance to SN is described in §6. Hydrodynamical modeling to estimate physical parameters is described in §7. A brief summary of the work is given in §8.

2 OBSERVATIONS

Broadband photometric data have been collected in Johnson *BV* and Sloan *gri* systems using the Las Cumbres Observatory Global Telescope (LCOGT) network, description of instrument and telescopes are presented in Brown et al. (2013). We have also used ARIES 104-cm Sampurnanand Telescope (ST) and the 130-cm Devasthal Fast Optical Telescope (DFOT) to acquire broadband data in Johnson-Cousin *UBVRI* filters. The instrument details are presented in Bose et al. (2013) and Sagar et al. (2012). *Swift* UVOT has also observed SN 2013ab in ultra-violet (UV) and optical broadbands. A detailed description of data reduction and derivation of photometric magnitudes are given in Appendix A.

Low resolution spectroscopic observations have been carried out at 25 phases from 2 to 184d after explosion; 12

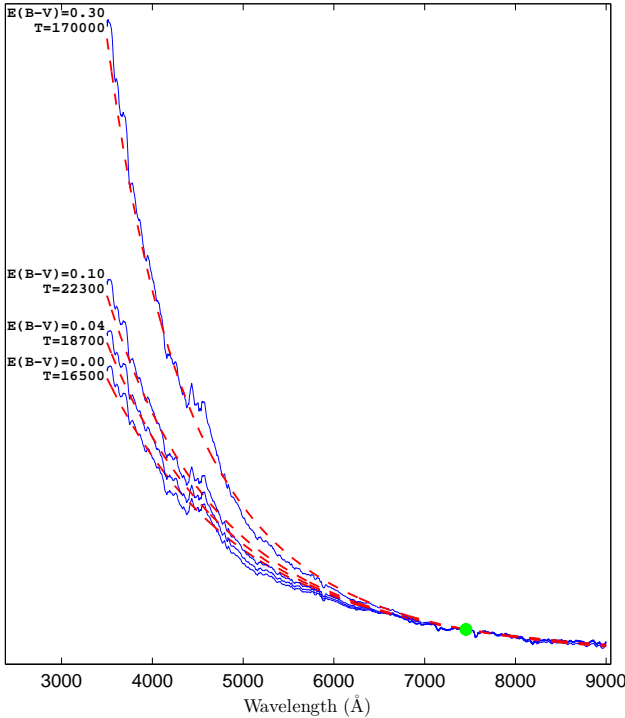


Figure 2. The spectral energy distribution of SN 2013ab at 2.2d is compared with a blackbody function (dotted line). The fluxes are normalized relative to an arbitrary line-free region in the spectra marked with a green filled circle. Temperature units are kelvin (K) and $E(B - V)$ in magnitude.

epochs of data were collected using Floyds spectrograph on Faulkes Telescope North (FTN), 6 epochs on Faulkes Telescope South (FTS), 5 epochs using HFOSC on Himalayan Chandra Telescope (HCT) and 2 epochs using the B&C spectrograph mounted on Galileo Telescope in Asiago. The data reduction process is given in Appendix B and the journal of spectroscopic observations in Table B1.

3 EXTINCTION AND DISTANCE

In order to derive intrinsic properties of the explosion, the line-of-sight reddening of SN 2013ab due to interstellar dust in both the Milky Way and the host galaxy should be known accurately. Using all-sky dust-extinction map of Schlafly & Finkbeiner (2011)¹, we adopt the following value of Galactic reddening: $E(B - V)_{\text{MW}} = 0.0234 \pm 0.0002$ mag.

One of the widely adopted techniques for reddening estimate is using the narrow NaI D interstellar absorption dips. The equivalent width (EW) of NaI D absorption feature is found to be correlated with the reddening $E(B - V)$ estimated from the tail of SN Ia colour curves (Barbon et al. 1990; Turatto et al. 2003). However in our low resolution set of spectra, we did not identify any NaI D absorption feature indicating that extinction due to the host galaxy is very low and of the order of Galactic reddening. To further constrain $E(B - V)$ due to the host galaxy, we implement “colour-method” (Olivares et al. 2010), which assumes that

at the end of plateau phase the intrinsic $(V - I)$ colour is constant. Thus, it is possible to obtain the host colour excess from observed $(V - I)$ colour and relate it to the visual extinction. The relation found by Olivares et al. (2010) is :

$$A_V(V - I) = 2.518[(V - I) - 0.656] \quad (1)$$

$$\sigma_{(A_V)} = 2.518 \sqrt{\sigma_{(V - I)}^2 + 0.053^2 + 0.059^2} \quad (2)$$

Using the mean $(V - I)$ colour within 78-82 d (corresponds to the end of plateau phase), and correcting it for Galactic reddening, we obtain $A_{V_{\text{host}}} = 0.0624 \pm 0.2060$ mag which corresponds to $E(B - V)_{\text{host}} = 0.0201 \pm 0.0664$ mag assuming total-to-selective extinction $R_V = 3.1$. Hereafter, we adopt a total $E(B - V) = 0.044 \pm 0.066$ mag along the line of sight to SN 2013ab providing a total $A_V = 0.14 \pm 0.21$ mag.

To seek further justification of the derived $E(B - V)$ we look into the earliest spectra at 2.2 d. At early phases the spectral energy distribution (SED) can be well approximated as a blackbody. Hence we de-redden the spectra with different values of $E(B - V)$ and estimate corresponding blackbody temperatures (see Fig. 2). For $E(B - V) = 0.30$ mag we obtain an unphysically high temperature of 170 kK. The theoretical modelling of Dessart & Hillier (2006); Bersten et al. (2011) indicate that for a 2.2d old type IIP SN, the temperature must be around 25-30 kK. Our blackbody fit to the spectra with $E(B - V) = 0.10$ mag results in a temperature estimate of 22.3 kK. This is consistent with the values predicted by theoretical modeling. Also we estimate a temperature of 18.7 kK corresponding to our adopted $E(B - V) = 0.044$ mag. This analysis provides an approximate upper limit of $E(B - V) = 0.10$ mag which is consistent with the adopted reddening value determined using colour-method.

A number of distance estimates to NGC 5669 using the Tully-Fisher method are available in the literature with a wide variation in values ranging from 18 to 32 Mpc. Hence to seek for a reliable estimate, we applied EPM to the SN and derived a distance of 24.26 ± 0.98 Mpc. The detailed EPM analysis will be discussed in §6. We adopt the distance to host galaxy to be 24.0 ± 0.9 Mpc which is the weighted mean of EPM and two other recent Tully-Fisher estimates from the literature, viz. Theureau et al. (2007) (25.23 ± 4.65 Mpc) and Tully et al. (2009) (19.67 ± 3.35 Mpc), assuming $H_0 = 73 \text{ km s}^{-1} \text{Mpc}^{-1}$, $\Omega_m = 0.27$, $\Omega_\Lambda = 0.73$.

4 OPTICAL LIGHT CURVE

4.1 Apparent magnitude light curves

Photometric measurements in Johnson-Cousins *UBVRI* and SDSS *gri* are available at 136 phases from 1 to 189d after the explosion, with a stringent non-detection at -1d. Additional 25 epoch observations are from *Swift* UVOT in all six UVOT filters. The resulting light curves are shown in Fig. 3 and data is tabulated in Table A1.

The early light curve initially shows a sharp rise in *r* band, which is also visible in all other optical bands as well, but only during first few phases. Then the light curve declines slowly until the end of plateau-phase. Since 95d, a steep decline to the radioactive nebular tail follows. After

¹ <http://irsa.ipac.caltech.edu/applications/DUST/>

that, since ~ 113 d, the light curve settles on to this relatively slower declining phase. Observations in the UVOT bands do not show any initial rise in the light curve, although observations started with the same delay as the optical bands (+4d). The early peak is found to occur at 6.4, 7.2, 7.8, 8.3, 8.3, 7.8, 8.4 and 7.8d in *UBVRIgri* bands respectively, with uncertainties of about 1d. This is consistent with most fast-rising SNe (e.g. SN 2005cs, Pastorello et al. 2009), and is significantly different from some SNe which exhibit a slow-rising early phase light curve (see e.g. the delayed *V*-band maximum attained at 16d in SN 2006bp (Quimby et al. 2007); 13d in SN 2009bw (Inserra et al. 2012b); and 15d in SN 2012aw (Bose et al. 2013)).

The decline rates after the initial maximum to the plateau-end in *UBVRIgri* are 7.60, 2.72, 0.92, 0.59, 0.30, 1.68, 0.77, 0.51 mag 100 d^{-1} respectively. This is steeper than the values reported for SN 1999em (Leonard et al. 2002b), SN 1999gi (Leonard et al. 2002a) and SN 2012aw (Bose et al. 2013). For example in the *UBV*-bands, SN 2012aw experienced a decline rate of 5.60, 1.74, 0.55 mag 100 d^{-1} . However, the decline rate of SN 2013ab is similar to that of SN 2004et (2.2 mag 100 d^{-1} in *B* band; Sahu et al. 2006). During the nebular phase, the decline rate (mag 100 d^{-1}) of the light curves are estimated to be 0.36, 0.97, 0.76, 0.66 and 1.16 for *BVgri* respectively.

SN 2013ab is luminous in the UVOT UV bands at early phases, but it declines steeply at a rate of 0.169, 0.236 and 0.257 mag d^{-1} in *uvw1*, *uvw2* and *uvm2* bands respectively. After 30d, the light curves settle on a slow-declining plateau until ~ 103 d corresponding also with the end of *Swift* UVOT observations. SN 2012aw is the only known SN which shows a UV plateau (Bayless et al. 2013) similar to that observed in SN 2013ab. Although, a UV plateau is expected, not many type II SNe have been observed so far at these wavelengths until relatively late phases. This is possibly because of their low apparent brightness due to large distance and extinction, making them unsuitable for UVOT detections. However, these limitations did not hinder SN 2013ab making this event as one of the best observed SNe IIP in the UV domain.

4.2 Absolute magnitude and colour evolution

The *V*-band absolute light curve of SN 2013ab is shown in Fig. 4, and is compared with those of other well-studied type IIP SNe. All data are corrected for their corresponding distances and extinction values. SN 2013ab is compared with the normal SNe 1999em, 1999gi, 2004dj, 2004et and 2012aw; the subluminous SN 2005cs and the photometrically peculiar SN 1987A. The comparison shows that the *V*-band mid-to-late plateau absolute magnitude of SN 2013ab is very similar to those of SNe 1999em and 2012aw. However the plateau light curve decay rate, especially during the early-plateau (from 10 to 50d) phase is significantly larger than those of SNe 1999em and 2012aw (by 1.58 and 2.61 times respectively), although later on (during late-plateau phase) the slopes are somewhat similar. The decay rate of the early-plateau light curve is as high as 1.58 mag 100 d^{-1} , which is significantly higher than that of the late-plateau light curve (0.49 mag 100 d^{-1}). The nebular-phase light curve evolution follows a decay rate of 0.97 mag 100 d^{-1} which is similar to those of other SNe in our comparison

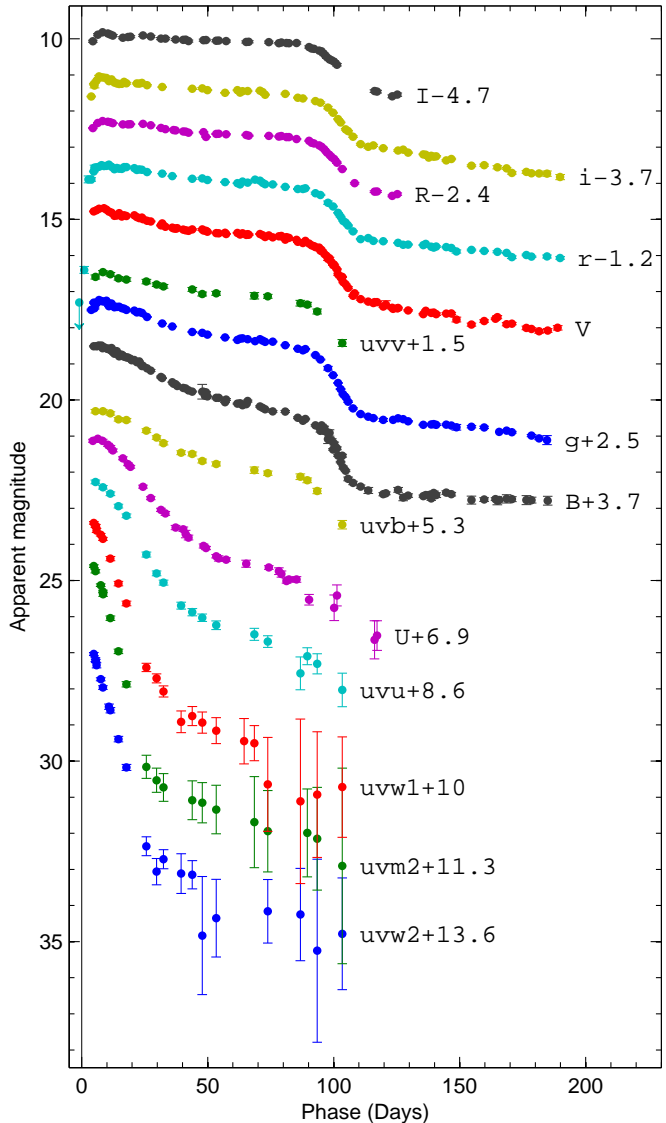


Figure 3. The photometric light curve of SN 2013ab in Johnson-Cousins *UBVRI*, SDSS *gri* and *Swift* UVOT bands. The light curves are shifted arbitrarily for clarity. The large errors in late UV data points are due to faint SN flux extracted after subtracting host background.

sample. This is consistent with the expected decay rate of the ^{56}Co to ^{56}Fe (0.98 mag 100 d^{-1}). The mid-plateau absolute magnitude is $M_V^p = -16.7$ mag, categorizing SN 2013ab as a normal type IIP event (Patat et al. 1994). This magnitude make SN 2013ab significantly brighter than subluminous class of events like SN 2005cs ($M_V^p \sim -15$ mag; Pastorello et al. 2009). Another noticeable difference with the compared SNe is the relatively shorter plateau duration, ~ 78 d in SN 2013ab, in contrast to ~ 90 d and 92d for SNe 1999em and 1999gi respectively. Anderson et al. (2014b) found an anti-correlation between the slope of early plateau and full-plateau duration for type II SNe, which is consistent with the faster decline but shorter plateau duration of SN 2013ab. However, it fits somewhat at the lower end of the scatter relation.

Swift UVOT absolute light curves (in *uvw*, *uvw1*, *uvm2*

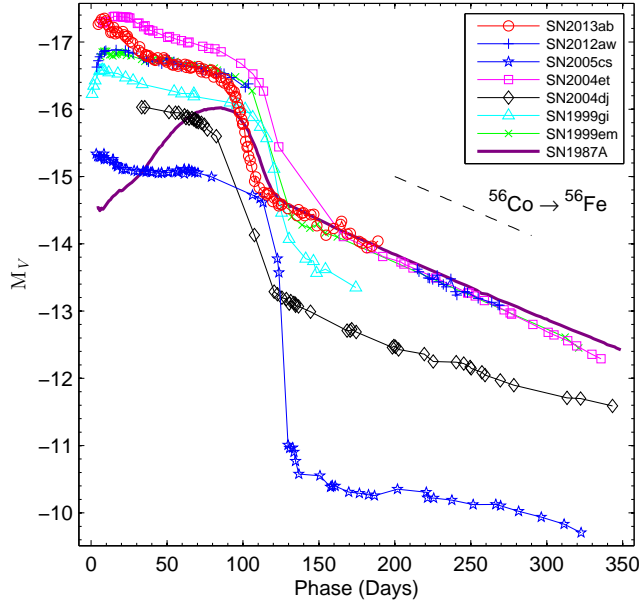


Figure 4. Comparison of the V -band absolute light curve of SN 2013ab with those of other type IIP SNe. The exponential decline of the radioactive decay law is indicated with a dashed line. The time of explosion in JD-2400000, distance in Mpc, reddening $E(B-V)$ in mag and the reference for apparent V -band magnitude, respectively, are : SN 1999em – 51475.6, 11.7, 0.10, Leonard et al. (2002b); Elmhamdi et al. (2003b); SN 2004et – 53270.5, 5.4, 0.41, Sahu et al. (2006); SN 2005cs – 53549.0, 7.8, 0.11, Pastorello et al. (2009); SN 2004dj – 53187.0, 3.5, 0.07, Tsvetkov et al. (2008); SN 1987A – 46849.8, 0.05, 0.16, Hamuy & Suntzeff (1990); SN 1999gi – 51522.3, 13.0, 0.21, Leonard et al. (2002a); SN 2012aw – 56002.6, 9.9, 0.07, Bose et al. (2013).

and $uvw2$ bands) of SN 2013ab are shown in Fig. 5 and are compared with other well observed IIP SNe. Distance and extinction has been corrected for each of the events. For SN 2006at, extinction is not known, hence a minimal reddening has been adopted accounting only for Milky Way extinction. SN 2013ab is on the brighter end among the compared events. Most SNe were not detected in UV after about a month, this is primarily due to large distances and extinction values. Both of these factors being not a major issue in SN 2013ab, which has been in fact observed for more than 100d. SNe 2012aw and 2013by are comparable with SN 2013ab in terms of data coverage and clear detection of a plateau in the UV domain. The plateau is evident in all UV bands after 30d and follows a similar trend as that observed in SN 2012aw.

The broadband colour evolution provides important information about the temporal variation of the SN envelope properties. The expansion and cooling behavior of the envelope can be studied from the colour evolution at different phases. The intrinsic colour evolutions ($U-B$, $B-V$, $V-R$ and $V-I$) are shown in Fig. 6. All colours show a rapid evolution towards redder colours until ~ 50 d, due to a rapid cooling of fast expanding ejecta. Thereafter, they evolve relatively slowly until the onset of the nebular-phase. The colour evolution is very similar in other archetypal SNe IIP such as SN 1999em and SN 2012aw. The $(B-V)$ colour shows a

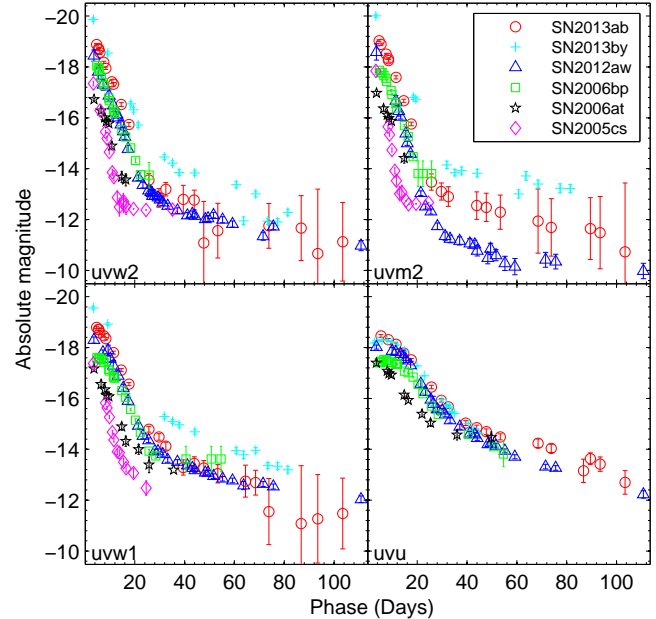


Figure 5. *Swift* UVOT UV absolute light curves of SN 2013ab, are compared with other well observed IIP SNe from UVOT. For the compared SNe, references for UVOT data, extinction and distance are: SN 2005cs – Brown et al. (2009); Pastorello et al. (2009), SN 2006at – Brown et al. (2009); Distance 65 Mpc; $E(B-V) = 0.031$ mag (only Galactic reddening Schlafly & Finkbeiner 2011), SN 2006bp – Dessart et al. (2008), SN 2012aw – Bayless et al. (2013); Bose et al. (2013), SN 2013by – Valenti et al. (2015).

bluer trend after 120d, when the nebular-phase begins. In this phase, the ejecta become sufficiently optically thin to allow photons from radioactive decay of ^{56}Co to ^{56}Fe to escape.

To have an idea of the temporal evolution of temperature and photospheric radius, we fit blackbody functions to the broadband optical fluxes (after correcting for total line-of-sight extinction). The blackbody radii are further corrected by dilution factors (using the prescription of Dessart & Hillier 2005a) to estimate photospheric radii (where optical depth is $\tau = 2/3$) rather than thermalization radii. The plot with the photospheric temperature and radius evolutions is shown in Fig. 7. The temperature drops very rapidly from 5 to 25d due to adiabatic cooling of the rapidly expanding envelope. Thereafter, the decline flattens as the SN progressively enters the nebular phase. The photospheric radius increases rapidly as the SN expands and thereafter the radius remains almost constant until around 85d, which marks the end of plateau phase. This apparent contradiction to the expansion is due to the fact, that with the fall of temperature the ionized hydrogen starts to recombine by depleting the free electrons thereby optically thinning the outer ejecta. This results to a receding photospheric layer on top of the expanding envelope, ultimately leading to an unchanged photospheric radius. After 85d the radius falls off very rapidly with the end of the hydrogen recombination. During this phase, the ejecta become cooler and almost optically thin leaving behind no free electrons.

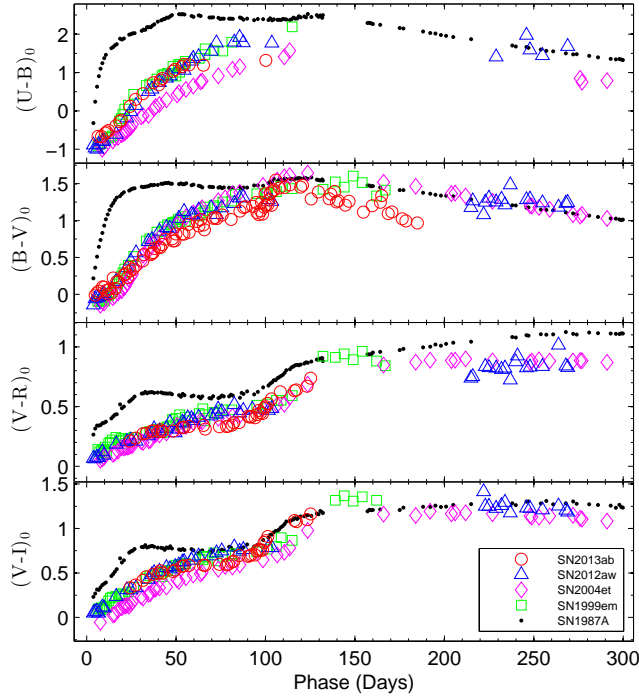


Figure 6. The evolution of intrinsic colours of SN 2013ab is compared with those of other well-studied type IIP SNe 1987A, 1999em, 2004et and 2012aw. Reference for data are the same as in Fig. 4.

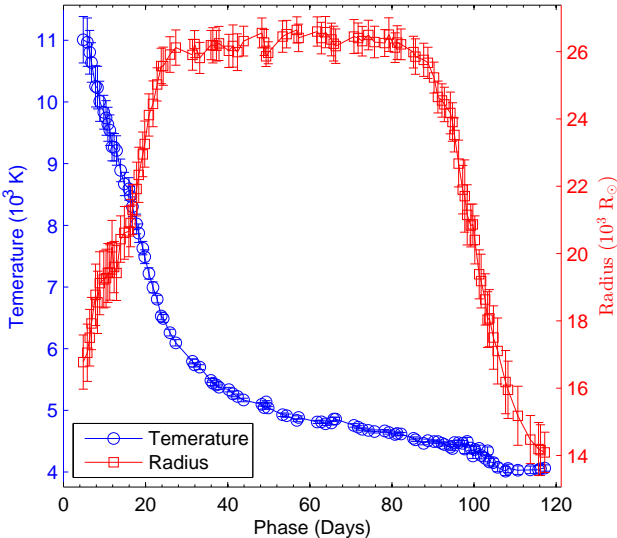


Figure 7. The evolutions of temperature and radius in SN 2013ab, as derived from blackbody fits to the observed fluxes in the optical range (0.36–0.81 μm).

Moreover, the dilution factor corrections are no longer applicable as radiation does not have thermal origin.

4.3 Bolometric light curve

Pseudo-bolometric luminosities have been computed at all phases adopting the same method as described in Bose et al.

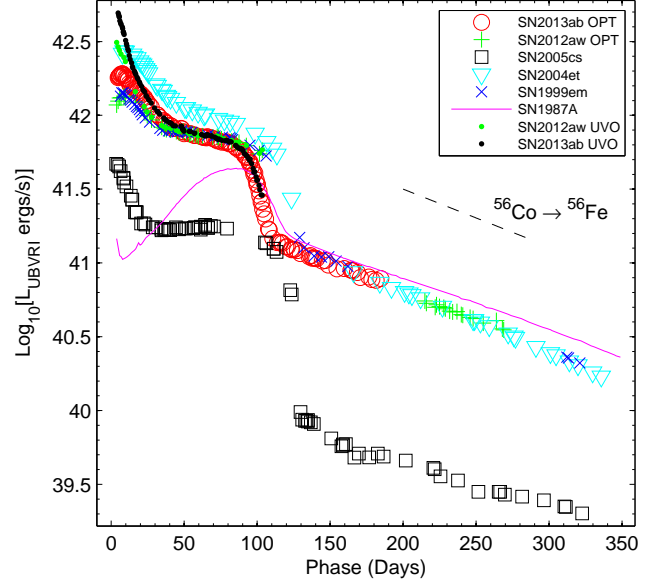


Figure 8. The $UBVRI$ pseudo-bolometric light curve of SN 2013ab is compared with those of other well-studied SNe. Light curves with added UVOT UV contributions are also shown for SN 2013ab and SN 2012aw (labeled as UVO). The adopted distances, reddening and time of explosion values are same as in Fig. 4. The exponential decline of the radioactive $^{56}\text{Co} \rightarrow ^{56}\text{Fe}$ is shown with a dashed line.

(2013), i.e. by constructing a SED from the extinction corrected photometric fluxes which are semi-deconvolved from broadband filter responses. At early phases ($\leq 30\text{d}$), when the SN is hot, the bolometric fluxes are dominated by the UV bands. At later phases ($\geq 100\text{d}$) a major fraction of the bolometric contribution comes from infrared domain. The luminosity is computed within the optical domain (3335 – 8750 \AA), which includes $UBVRI$ and gri contributions. We have also used UVOT data in the bolometric luminosity computation which covers the wavelength range from the $uvw2$ to the I bands (1606 – 8750 \AA). The contribution from the UV fluxes yields a significantly higher value of the early luminosity.

In Fig. 8, we plot the optical pseudo-bolometric luminosities of SN 2013ab along with other well-studied objects, including SNe 1987A, 1999em, 2004et, 2005cs, 2012aw. To have homogeneity in the comparison of bolometric light curves, all luminosities have been computed using the same algorithm and wavelength range. We also include UV-Optical bolometric light curves of SNe 2013ab and 2012aw for comparison. The bolometric luminosity declines rapidly by 0.4 dex from 8 to 50d and then goes down further but slowly by 0.1 dex until 85d. It is evident from the comparison that the plateau bolometric luminosity of SN 2013ab is close to those of SNe 1999em and 2012aw but with a much steeper decline rate of the light curve during the plateau. However, the decline rate and shape of light curve matches well with that of SN 2004et. The UV-optical bolometric light curve of SN 2013ab also shows a sharp decline by 0.8 dex during the first 50d, which is steeper than that observed for SN 2012aw. Thereafter, it declines relatively slowly and coincides with the optical light curve. The tail bolometric luminosity is

similar to those of SNe 1999em, 2004et and 2012aw, and the slope of the tail is nearly identical to that expected for ^{56}Co to ^{56}Fe radioactive decay. Since this powers the tail luminosity, it is directly proportional to the amount of radioactive ^{56}Ni synthesized during the explosion.

4.4 Mass of nickel

The radioactive ^{56}Ni is produced in CCSNe by the explosive nucleosynthesis of Si to O (Arnett 1980). Thus the nebular-phase light curve is mainly powered by the radioactive decay of ^{56}Ni to ^{56}Co and ^{56}Co to ^{56}Fe , with e -folding time of 8.8d and 111.26d respectively emitting γ -rays and positrons. Hence the tail luminosity will be proportional to the amount of synthesized radioactive ^{56}Ni . The mass of ^{56}Ni produced by SN 1987A has been determined with a fair degree of accuracy to be $0.075 \pm 0.005 \text{ M}_\odot$ (Arnett 1996). By comparing the bolometric luminosity of SN 2013ab with that of SN 1987A at similar phases, we can infer the amount of synthesized ^{56}Ni in SN 2013ab. Although UVOIR bolometric light curve is available for SN 1987A, we preferred to use our $UBVRI$ pseudo-bolometric light curve computed using same algorithm that is used for SN 2013ab to have uniformity in the comparison. We estimated the $UBVRI$ bolometric luminosity of SN 2013ab at 170d, by making a linear fit over 160 to 181d, to be $8.41 \pm 0.72 \times 10^{40} \text{ erg s}^{-1}$. Likewise, we estimated the luminosity of SN 1987A at similar phases to be $9.93 \pm 0.04 \times 10^{40} \text{ erg s}^{-1}$. The ratio of SN 2013ab to SN 1987A is found to be 0.847 ± 0.073 , which gives a $M_{\text{Ni}} = 0.064 \pm 0.006 \text{ M}_\odot$ for SN 2013ab.

Assuming the γ -photons emitted from the radioactive decay of ^{56}Co thermalize the ejecta, the ^{56}Ni mass can be independently estimated from the tail luminosity, as described by Hamuy (2003).

$$M_{\text{Ni}} = 7.866 \times 10^{-44} \times L_t \exp \left[\frac{(t_t - t_0)/(1+z) - 6.1}{111.26} \right] \text{ M}_\odot,$$

where t_0 is the explosion time, 6.1d is the half-life of ^{56}Ni and 111.26d is the e -folding time of the ^{56}Co decay. We compute the tail luminosity L_t at 8 epochs between 158 and 182d from the V -band data, corrected for distance, extinction and a bolometric correction factor of 0.26 ± 0.06 mag during nebular phase (Hamuy 2003). The weighted mean value of L_t is $18.43 \pm 0.83 \times 10^{40} \text{ erg s}^{-1}$, corresponding to a mean phase of 172d. This tail luminosity corresponds to a value of $M_{\text{Ni}} = 0.064 \pm 0.003 \text{ M}_\odot$.

Elmhamdi et al. (2003a) has found a tight linear correlation between the $\log(M_{\text{Ni}})$ and the plateau V -band absolute magnitude at $(t_i - 35)$ epoch, where t_i is inflection time. Which is defined as the moment when the slope of the light curve in the transition phase is maximum. For SN 2013ab light curve, we constrained $t_i = 102.99 \pm 0.02$ d. Following the above mentioned correlation we obtain $M_{\text{Ni}} = 0.066 \pm 0.002 \text{ M}_\odot$.

We adopt the mass of synthesized ^{56}Ni in SN 2013ab to be $0.064 \pm 0.006 \text{ M}_\odot$, which is derived from the first method, and is found to be consistent with that obtained from the subsequent two methods described here. We anticipate that the estimated ^{56}Ni mass for SN 2013ab is almost equal to that obtained for SNe 2012aw, 2004et and 1999em. Whereas

for sub-luminous SN 2005cs, ^{56}Ni mass is much less than SN 2013ab.

5 OPTICAL SPECTRA

5.1 Key spectral features

The spectroscopic evolution of SN 2013ab is presented in Fig. 9. Preliminary identification of spectral features has been done as in previous studies of IIP SNe (e.g. Leonard et al. 2002b; Bose et al. 2013). Early spectra, viz. 2.2d and 3.2d, shows featureless blue continuum with a broad and shallow P-Cygni dip detected near 4380 Å which is supposedly $\text{He II } \lambda 4686$, which is blue shifted by about 19500 km s^{-1} . Detection of such He II features has been reported in several early SN spectra (Fassia et al. 2001; Quimby et al. 2007; Inserra et al. 2013; Shivvers et al. 2014; Pastorello et al. 2015). The 8.2d spectrum also primarily shows blue continuum, although with developing $\text{H}\beta$, He I and $\text{H}\alpha$ lines. The He I feature completely disappears after 18d and at similar position Na I D profile starts to emerge since the 43d spectrum.

The spectra from 12 to 18d mark the transition phase from a hot to cool SN envelope, when photosphere begins to penetrate the deeper Fe-rich ejecta. These spectra mark the emergence of other lines from heavier atomic species, such as calcium, iron, scandium, barium, titanium and neutral sodium. Among these lines, $\text{Fe II } \lambda 5169$ appear during the early plateau phase (12d), whereas weaker lines start to emerge at the beginning of late plateau phase (18d). Na I D doublet $\lambda\lambda 5890, 5896$ and Ca II triplets $\lambda\lambda 8498, 8542, 8662$ are feebly traceable from 31d, and becomes prominent since the 43d spectrum. All weak and blended lines are seen to evolve and appear prominently by the end of plateau phase (82.1d). The following spectrum (88.3d) marks the onset of plateau to nebular transition. All subsequent spectra up to 118.1d are representative of the early nebular phase, when the outer ejecta has become optically thin. Fig. 10 compares SN 2013ab spectra with sample of archetypal IIP events at four different epochs, viz. early and hot plateau phase at 8d; cooler plateau phase at 31 and 74d; and nebular phase at 174d. SN 2013ab spectra show features identical to those of our comparison sample of normal events. The nebular spectrum at 183d is shown in Fig. 11 with preliminary identification of nebular lines typical of SNe IIP. This spectrum is mostly dominated by emission features of $[\text{O I}] \lambda\lambda 6300, 6364$, $[\text{Ca II}] \lambda\lambda 7291, 7324$, and $[\text{Fe II}] \lambda\lambda 7155, 7172$. In addition, permitted emission lines of H I , $\text{Na I } \lambda\lambda 5890, 5896$ doublet and the Ca II NIR triplet are still detected.

5.2 SYNOW modelling of spectra

Spectra of SN 2013ab have been modeled with **SYNOW** 2.3² (Fisher et al. 1997, 1999; Branch et al. 2002) for preliminary line identification and velocity estimates. SYNOW is a parametrized spectrum synthesis code which employs Sobolev approximation to simplify radiation transfer equations, assuming spherically symmetric supernova ejecta which expand homologously. Despite of the simplified LTE

² <http://www.nhn.ou.edu/~parrent/synow.html>

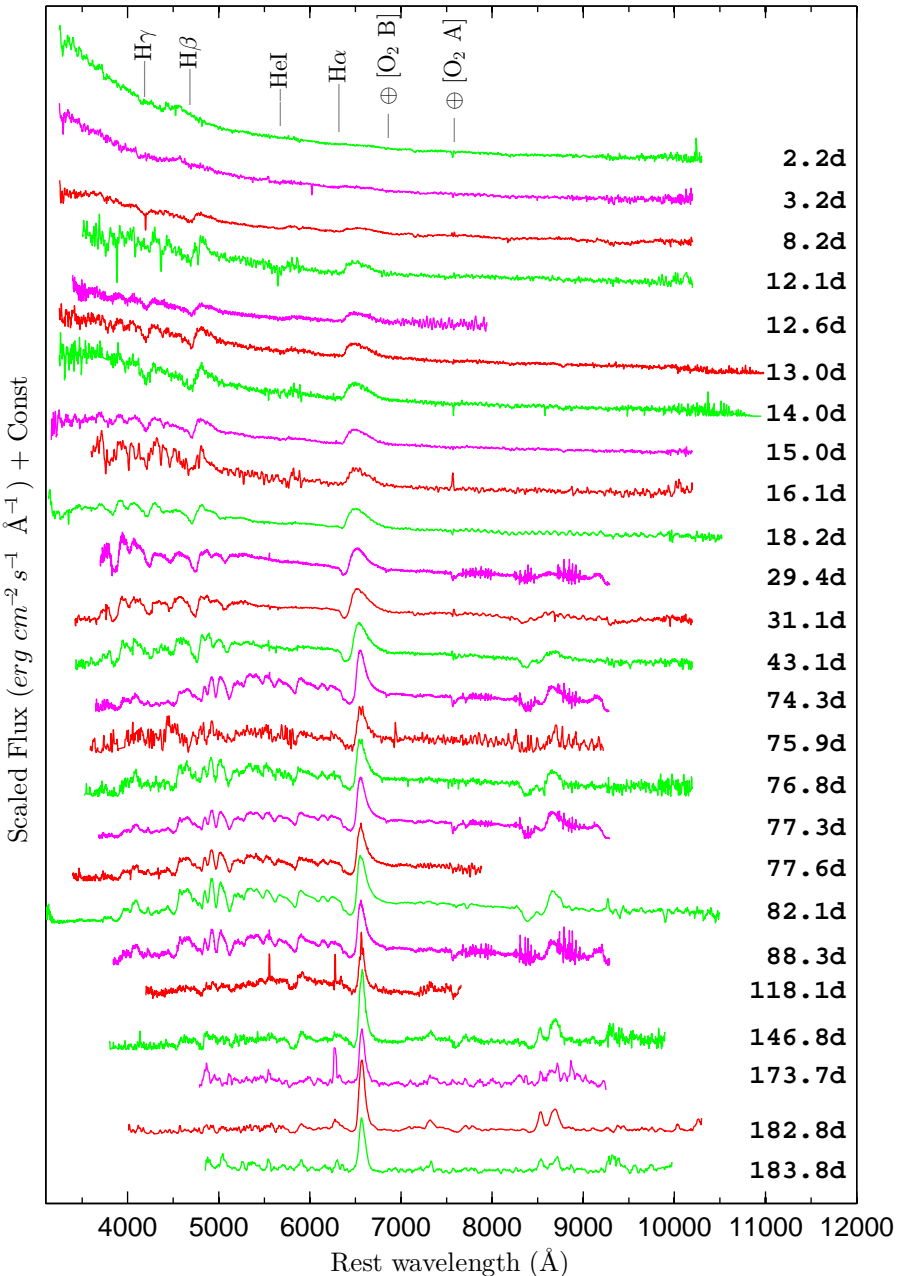


Figure 9. The Doppler-corrected spectra of SN 2013ab are shown at 14 phases from 7d to 270d. Prominent P-Cygni profiles of hydrogen ($H\alpha$, $H\beta$, $H\gamma$) and helium (HeI $\lambda 5876$) lines are marked. The telluric absorption features are indicated with the \oplus symbol. The portions of spectra at the extreme blue and red ends have poor signal-to-noise ratios.

atmosphere assumption in SYNOW, it is capable to produce P-Cygni profiles like those produced in the expanding photosphere of a SN. SYNOW has been implemented on several recent SNe studies (e.g. Inserra et al. 2012a; Bose et al. 2013; Milisavljevic et al. 2013; Bose & Kumar 2014; Takáts et al. 2014; Marion et al. 2014) for line identification and estimation of line velocities. We tried three different options for optical depth profiles (viz. Gaussian, exponential and power law), no significant differences were noticed. However, while matching absorption minimum, the exponential profile, $\tau \propto \exp(-v/v_e)$, where v_e , a profile fitting parameter, e-folding velocity, was found to be the most suitable and is

adopted here for each individual atomic species. One important aspect of SYNOW modeling is the concept of detachment of an ion. When the minimum velocity of a line-forming layer is higher than that of the photospheric layer, the ion is said to be detached, which results into flat topped emission and blueshifted absorption counterpart of the line profile in synthetic spectra produced by SYNOW. This becomes important for $H I$ lines as they are essentially formed at much higher velocities than photospheric velocities. Therefore, only the detached scenario for $H I$ reliably fits the blue-shifted absorption trough in the observed spectra.

The observed spectra are dereddened and doppler-

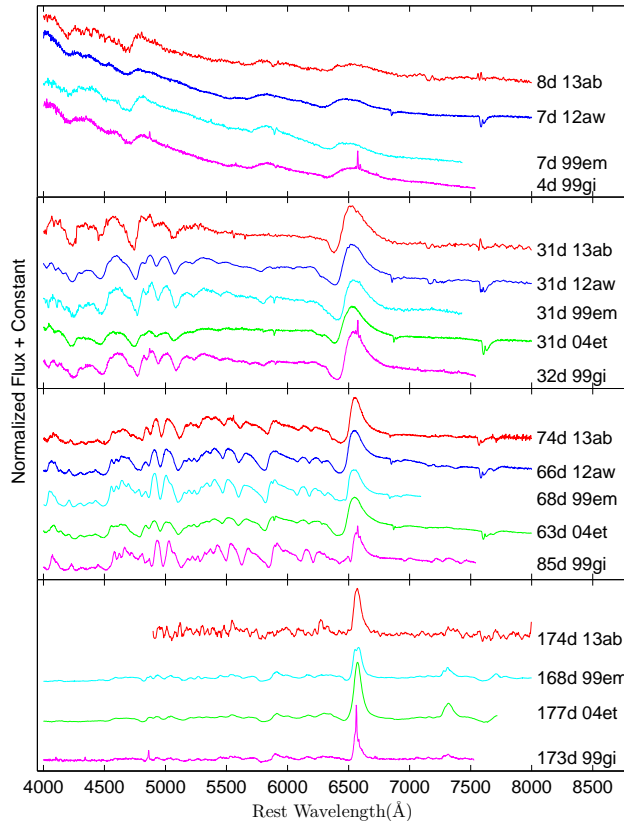


Figure 10. Comparison of early (8d), plateau (31d, 74d) and nebular (174d) phase spectra of SN 2013ab with those of other well-studied type IIP SNe 2012aw (Bose et al. 2013), 1999em (Leonard et al. 2002b), 1999gi (Leonard et al. 2002a), 2004et (Sahu et al. 2006; Maguire et al. 2010). Observed fluxes of all the SNe are corrected for extinction and redshift (adopted values same as in Fig. 4).

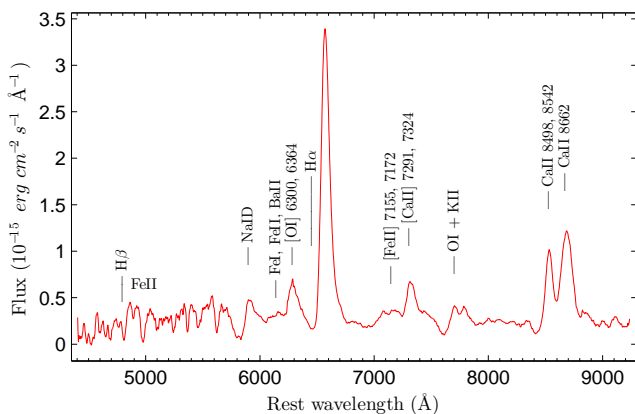


Figure 11. Line identification in the nebular phase spectrum of SN 2013ab (183d).

corrected before modelling with SYNOW. T_{bb} is supplied as a model input parameter which is actually the blackbody temperature to produce the underlying LTE continuum of synthetic spectra. For this reason, the observed spectral continuum is well matched at early phases, whereas at later phases this is a poor match with the model as SN emission

significantly deviates from LTE assumption. Fig. 12 shows the observed spectrum at 77.3d with our best-fit model. A set of atomic species (H I, He I; Fe II; Ti II; Sc II; Ca II; Ba II; Na I; Si II; O I; N I) has been incorporated to generate the synthetic spectrum. The model spectrum can very well reproduce most of the blended line profiles; v_{ph} is optimized to match the Fe II multiplet ($\lambda\lambda$ 4924, 5018, 5169), whilst the H I velocities are always dealt as a detached scenario.

Line velocities for H β , He I and Fe II are estimated from all spectra. The model fit is optimized for velocity locally around the respective lines of interest. Fitting is done locally to avoid any bias in velocity estimation, which may be imposed while accounting for entire spectrum due to other lines at different velocities. In Table 2, SYNOW estimated velocities for a few representative lines in the plotted spectral sequence are shown. Although Fe II line impression is detectable since 12d, we model those lines only from 29d onwards, as in earlier spectra Fe II triplet is either not full developed or only detectable Fe II λ 5169 is too weak to model. SYNOW modelling is done until 77d, because after 78d spectra are limited because of low signal-to-noise ratio (SNR). In such low SNR spectra SYNOW may not provide any better estimation of line velocities than absorption-minima position measurements.

5.3 Evolution of spectral lines

The evolution of spectral features provides important clues about the interaction of expanding ejecta with the circumstellar material, formation of dust in the ejecta and geometrical distribution of the ejecta. To illustrate the evolution of individual lines, in Fig. 13 selected regions of spectra are plotted in the velocity domain corresponding to the rest wavelengths of H β , Na I D and H α . There is no clear evidence of spectral lines in the early spectra (2.2 and 3.2d), except for a shallow and broad He II (λ 4686) feature near 4380Å. The blue-shifted absorption troughs of the P-Cygni profiles give direct estimate of expansion velocity of the ejecta. The emission peaks are also seen to be blue-shifted. The amount of blue-shift decreases with the decline of the expansion velocity and settles to the rest velocity while the SN enters the nebular phase. This is a generic feature seen in SN spectra, mostly at early phases; see, e.g., SNe 1987A (Hanuschik & Dachs 1987), 1998A (Pastorello et al. 2005), 1999em (Elmhamdi et al. 2003b), 2004et (Sahu et al. 2006) and 2012aw (Bose et al. 2013). Blue-shifted emission peaks are explained by the diffused reflection of photons from expanding SN envelope (Chugai 1988) which is in contrast to the pure-absorption model of expanding atmosphere ensuing un-shifted emission peaks. However, recent study by Anderson et al. (2014a) suggests that these features are tied with the density structure of ejecta which in turn controls the amount of occultation of the receding part of ejecta, resulting in biasing of the emission peak. Such features are well reproduced by non-LTE models like CMFGEN (Dessart & Hillier 2005c). The evolution of blue-shifted peaks are clearly seen in H α , whilst other lines emission peaks are heavily contaminated by P-Cygni the absorptions from other adjacent lines. The emission peak blue-shift for H α is found to be as high as ~ -5000 km s $^{-1}$ at 8.2d and then progressively decreases (4400 km s $^{-1}$ at 12d and 2300

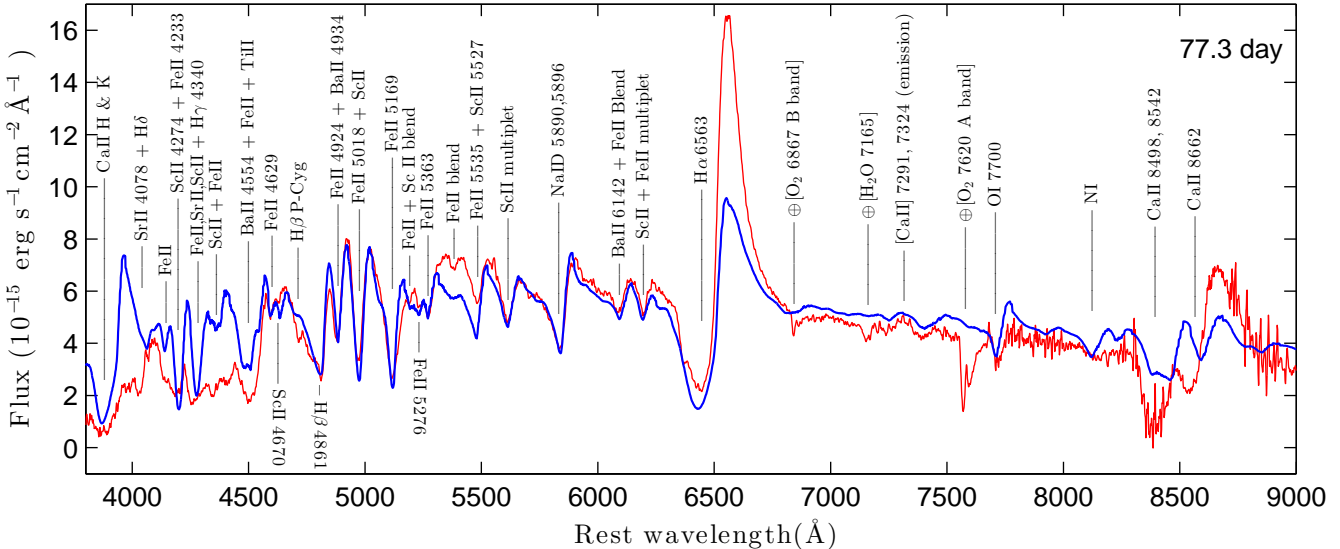


Figure 12. SYNOW modelling of the 77.3d spectrum of SN 2013ab. A SYNOW model spectrum is shown with thick solid line (blue), while the observed one is the thin solid line (red). Fluxes are corrected for interstellar extinction.

Table 2. The best-fit blackbody continuum temperature (T_{bb}) and line velocities of $H\beta$, $Fe\text{ II}$ ($\lambda\lambda 4924, 5018, 5169$) and $He\text{ I}$ $\lambda 5876$ as estimated from SYNOW modeling of the observed spectra of SN 2013ab. Velocities derived using lines of $Fe\text{ II}$ or $He\text{ I}$ are taken as representative of the velocity of photosphere (v_{ph}).

UT Date (yyyy-mm-dd)	Phase ^a (day)	T_{bb}^b (kK)	$v(He\text{ I})$ 10^3 km s^{-1}	$v(Fe\text{ II})$ 10^3 km s^{-1}	$v(H\beta)$ 10^3 km s^{-1}
2013-02-24.71	8.21	11.8	10.2 ± 0.3	-	10.4 ± 0.6
2013-02-28.59	12.09	9.6	10.1 ± 0.7	-	10.4 ± 0.6
2013-03-01.08	12.58	1.1	9.4 ± 0.4	-	10.3 ± 0.3
2013-03-01.50	13.00	9.9	9.0 ± 0.5	-	10.3 ± 0.2
2013-03-02.51	14.01	1.0	8.7 ± 0.9	-	10.2 ± 0.5
2013-03-03.51	15.01	9.2	9.0 ± 0.6	-	9.5 ± 0.2
2013-03-04.59	16.09	8.4	8.2 ± 0.8	-	9.3 ± 0.8
2013-03-06.71	18.21	8.5	8.3 ± 0.6	-	9.8 ± 0.4
2013-03-17.93	29.43	6.8	-	6.1 ± 0.3	7.0 ± 0.3
2013-03-19.63	31.13	5.9	-	6.5 ± 0.4	7.5 ± 0.2
2013-03-31.58	43.08	5.6	-	4.9 ± 0.4	6.0 ± 0.3
2013-05-01.84	74.34	5.0	-	3.1 ± 0.3	3.1 ± 0.4
2013-05-03.35	75.85	5.2	-	-	-
2013-05-04.33	76.83	5.1	-	3.4 ± 0.4	3.8 ± 0.3
2013-05-04.85	77.35	5.2	-	2.9 ± 0.3	3.0 ± 0.3

^a With reference to the time of explosion JD 2456340.0

^b Best-fit blackbody temperature at the photosphere to match the continuum in the observed spectrum.

km s^{-1} at 29.4d) down to almost zero velocity at 88.3d, corresponding to the end of plateau phase.

Similar to $H\alpha$, $H\beta$ are seen to evolve all throughout the spectral evolution (see Fig. 13). However, 18d onwards, the red side of $H\beta$ emission profiles are found to be significantly dominated by emerging $Fe\text{ II}$ lines. All three $Fe\text{ II}$ lines ($\lambda\lambda 4924, 5018, 5169$) are seen to have fully appeared in 31d spectrum, which continues to evolve till the last observation. Traces of $He\text{ I}$ line are seen in early spectra, which disappears after 18d. At similar position $Na\text{ I}$ D profile start to appear at 43d and it continues to evolve until last spectrum.

5.4 Ejecta velocity

The element distribution of the progenitor at the end of the sequence of nuclear burnings and before the SN explosion is stratified, with hydrogen being abundant in outermost layers and heavier elements (e.g. α -elements) towards the center and core being rich in iron. Thus it is expected that the expanding ejecta are constituted by layers of multiple elements and the so called “onion-like” structure. Therefore, different lines originate from different depths in the SN atmosphere. The photosphere is a region of special interest to study the kinematics and other related properties. The photosphere represents the layer of SN atmosphere where optical depth attains a value of $\sim 2/3$ (Dessart & Hillier 2005b). No sim-

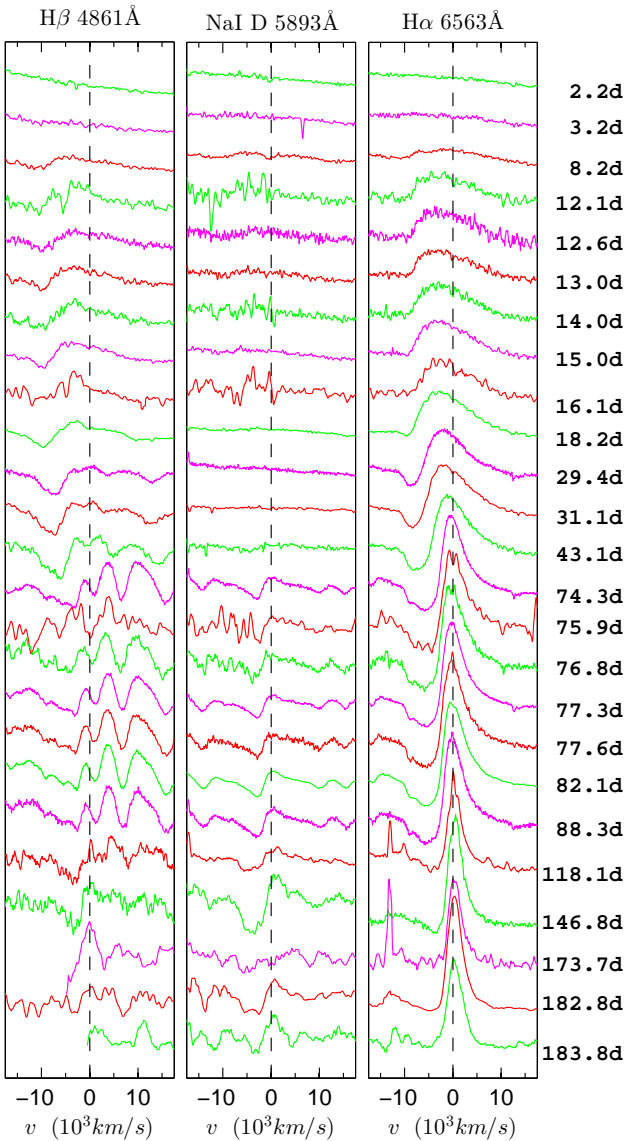


Figure 13. Evolution of the line profiles of $H\beta$, $NaI D$ and $H\alpha$ plotted at 25 epochs from 2d to 184d. The zero-velocity position is shown with a dotted line and the corresponding rest wavelength is indicated at the top.

gle spectral line can represent the true photospheric layer and its velocity. During the plateau phase, $Fe II$ ($\lambda\lambda 4924, 5018$ and 5169) or $Sc II$ lines are thought to be the best estimators for the photospheric velocity (v_{ph}), and at early phases when $Fe II$ lines are not strongly detected, the best proxy for v_{ph} is $He I$ or even $H\beta$ (Takáts & Vinkó 2012), at earlier phases.

Velocities can be estimated either by simply locating the blue-shifted absorption trough of the P-Cygni profiles or modeling the observed spectra where velocity is one of the input parameter. We have used both methods to estimate the velocities. SN spectral lines are often found to be blended with other lines in the neighborhood, as in case of $Fe II$ multiplets, blended with $Ti II$ and $Ba II$. This introduces some error, when lines velocities are estimated by locating the absorption minima, by simply fitting gaussian function

on these blended profiles, which is further exacerbated in low-resolution and low-SNR spectra. **SYNOW** being capable to reproduce P-Cygni profile for multiple lines of different ions simultaneously, it can easily reproduce line blending as observed in SN spectra. Thus we get a better handle while fitting the entire blended profile with **SYNOW** and so the velocity estimates are better and less prone to errors. More detailed discussion on applicability and merits of **SYNOW** velocity estimates over absorption minima method can be found in Takáts & Vinkó (2012) and Bose & Kumar (2014).

In order to estimate photospheric velocities from the model, **SYNOW**-generated synthetic spectra are locally fitted over $Fe II$ lines in the observed spectra. This was done to avoid any over- or under- estimation of velocities as each line of any atomic species originating from different layers. The attributed uncertainties are visually estimated by noting the deviation of model absorption trough from observed one. The model velocities listed in Table 2 are estimated only until 77.3d, since thereafter the spectra are limited by SNR and hence there is no advantage in using **SYNOW**-estimated velocities over the absorption minima method. The $Fe II$ velocities are estimated by assuming that the $Fe II$ $\lambda 4924$, $Fe II$ $\lambda 5018$, and $Fe II$ $\lambda 5169$ lines have velocities coincident with v_{ph} , whereas the Balmer $H I$ lines are treated as detached (with $v > v_{ph}$) (Branch et al. 2002; Bose et al. 2013). $He I$ line velocities have also been estimated as long as this ion can be traced in spectra (from 8.2 to 18.2 d).

The expansion velocities of $H\alpha$, $H\beta$, $He I$, $Fe II$ ($\lambda\lambda 4924, 5018$ and 5169), $Sc II$ $\lambda 6247$ and $Sc II$ $\lambda 4670$ have also been determined using **IRAF** by fitting the absorption trough with a Gaussian profile. The results are plotted in Fig. 14. It can be seen that $H I$ lines are formed at larger radii than $He I$ whereas $Fe II$ lines are formed at much smaller radii, having lower velocities. The $Sc II$ lines are formed at an even smaller radius. $Sc II$ lines are weak in strength and due to the limitation of our low SNR spectra, these lines are only detected during 77 to 147d.

Fig. 15 shows the comparison of photospheric velocity of SN 2013ab with those of other well-studied SNe 1987A, 1999em, 1999gi, 2004et, 2005cs and 2012aw. For the purpose of comparison, the absorption trough velocities have been used, taking the mean of $Fe II$ lines (or $He I$ lines at early phases where $Fe II$ lines are not detected). The velocity profile of SN 2013ab is very similar to those of other normal SNe IIP. On the other hand, the velocities of SN 2005cs and SN 1987A are significantly smaller than those of normal events including SN 2013ab. The shape and values of the SN 2013ab velocity profile is strikingly similar to those of SNe 2004et and 2012aw, whereas the velocities are consistently higher than SNe 1999gi and 1999em by $\sim 800 \text{ km s}^{-1}$.

6 EXPANDING PHOTOSPHERE METHOD

Expanding photosphere method (EPM) is a geometrical technique (Kirshner & Kwan 1974; Eastman et al. 1996) in which the angular radius is compared with physical radius of the SN photosphere to estimate its distance. Assuming homologous expansion of SN photosphere, the physical radius at any instant is approximated from expansion velocity (v_{ph}), and angular radius (θ) is estimated from blackbody fit corrected with the dilution factor (ξ) of Dessart & Hillier

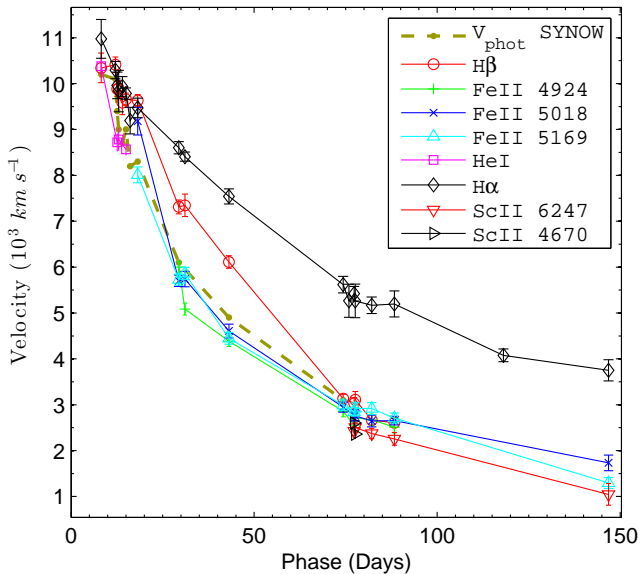


Figure 14. Evolution of the H α , H β , HeI, ScII and FeII line velocities. The velocities are estimated through the Doppler-shift of the absorption minima. The expansion velocities at the photosphere (v_{ph}) estimated from SYNOW fits of HeI line until 18d and simultaneous fits for FeII lines at later phases (see Table 2) are shown as a comparison.

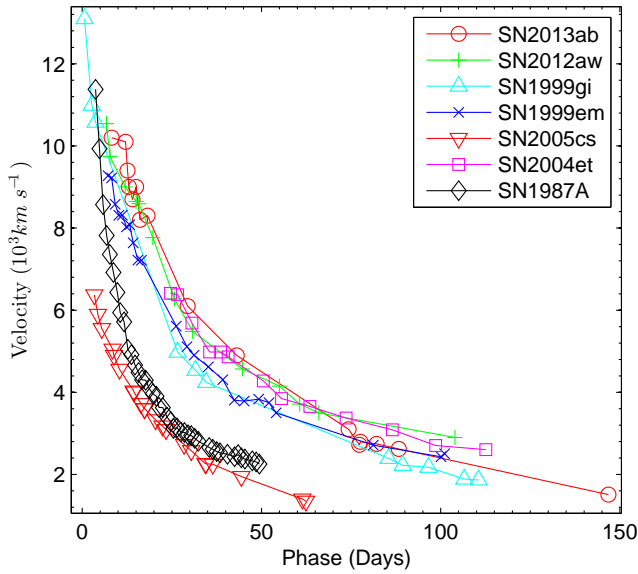


Figure 15. The evolution of photospheric velocity (v_{ph}) of SN 2013ab is compared with those of other well-studied SNe. The v_{ph} plotted here are the absorption trough velocities (from HeI lines at early phases, and FeII at late phases.)

(2005b) for non-LTE SNe atmosphere. Distance (D) and explosion epoch (t_0) are related with the quantity θ/v_{ph} at any given time t as,

$$t = D \left(\frac{\theta}{v_{ph}} \right) + t_0 \quad (3)$$

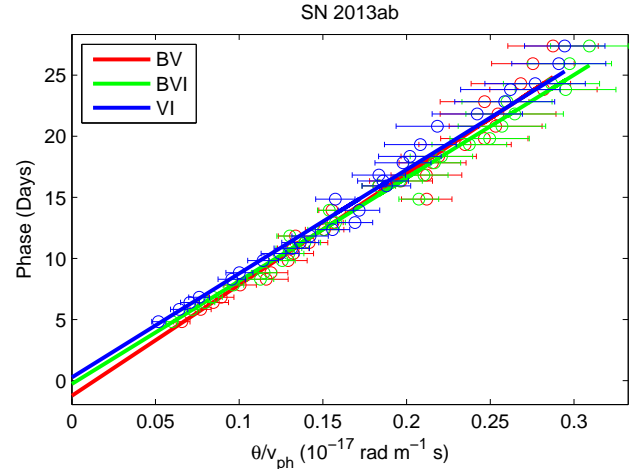


Figure 16. The EPM fit for SN 2013ab, using Dessart & Hillier (2005b) prescription for the dilution factor and using three filter sets.

Thus, the plot of t against θ/v_{ph} , yield distance as the slope and explosion epoch as the y-intercept.

EPM has been successfully applied to a considerably large sample of type IIP events by Jones et al. (2009) and Bose & Kumar (2014). The merits and limitations of the method has also been tested for multiple aspects. Here, we followed the same approach as described in Bose & Kumar (2014). It has also been shown that the two dilution factor prescriptions given by Hamuy et al. (2001) and Dessart & Hillier (2005a) have significant differences with the latter being more consistent with other redshift-independent distance estimates. In addition also the SYNOW-estimated velocities are better suited for such analysis. Taking into account all these factors, we have used the Dessart & Hillier (2005a) dilution factor prescription and SYNOW estimated velocities for EPM analysis. We also restricted our data set up to 30d only. We derived an EPM distance of 24.26 ± 0.98 Mpc which is the mean value for BV , BVI and VI band-sets (Fig. 16). The corresponding derived explosion epoch from EPM is $JD 2456339.59 \pm 0.76$ day, which is in good agreement with the uncertainty of adopted explosion epoch from observations (see §1). In principle we can constrain explosion epoch and keep distance as the only free parameter for the analysis. This yields a distance of 23.49 ± 0.77 Mpc. Since, the derived explosion epoch from unconstrained analysis is within the uncertainty of the observationally adopted explosion epoch, and the derived distances from constrained and unconstrained analysis are reasonably consistent within the limits of uncertainty, we prefer to adopt the EPM distance as derived from the unconstrained analysis. The EPM distance is found to be in good agreement with mean redshift independent distance estimates (24.9 ± 5.8 Mpc) listed in NED³ database for the galaxy NGC 5669.

³ NASA Extragalactic Database <http://ned.ipac.caltech.edu/>

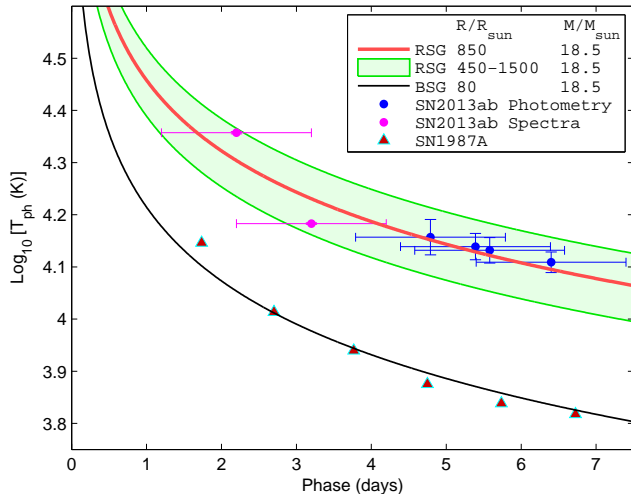


Figure 17. Constraining radius using Rabinak & Waxman (2011) prescription. The red solid line is the best fit for RGS of $850 R_{\odot}$ for SN 2013ab temperatures and the black solid line is for BSG of $80 R_{\odot}$ for SN 1987A temperatures (Menzies et al. 1987).

7 CHARACTERISTICS OF THE EXPLOSION

7.1 Radius of progenitor

During the shock breakout CCSNe heats the envelope to extremely high temperatures and then it cools down as the envelope expands. This temperature evolution depends on several parameters, viz. progenitor radius, opacity, explosion energy and mass. A simplified analytic formulation relating all these parameters has been determined by Rabinak & Waxman (2011). For a progenitor with larger radius, the envelope remains at a higher temperature for a longer time as compared to a progenitor with smaller radius. The temperature evolution is weakly dependent on the progenitor mass and energy, whereas radius and opacity are the dominating parameters. We computed blackbody temperatures from photometric fluxes and spectra and constrained progenitor radius by fitting the relation on these values (Fig. 17). We restricted our fits only within one week of the explosion as the relation is valid for the initial few days after the explosion. We adopted an optical opacity of 0.34 and a typical RSG density profile $f_p = 0.11$, however it is also noted that results are not very sensitive towards f_p . This analysis yields an initial radius of $750\text{--}950 R_{\odot}$ for the progenitor of SN 2013ab, adopting minimal line-of-sight extinction (see §3). The radius estimate suggests that the progenitor is possibly a large RSG. With increased extinction value the estimated radius would increase even further.

7.2 Hydrodynamical modelling

With the same well-tested approach adopted for other observed SNe (e.g. SNe 2007od, 2009E, 2009N, 2012A, and 2012aw; see Inserra et al. 2011; Pastorello et al. 2012; Takáts et al. 2014; Tomasella et al. 2013; Dall’Ora et al. 2014), we constrain the main physical properties of SN 2013ab at the explosion (namely the ejected mass, the progenitor radius and the explosion energy) through the hydro-

dynamical modelling of the main observables (i.e. bolometric light curve, evolution of line velocities and continuum temperature at the photosphere).

According to this approach, a simultaneous χ^2 fit of the above mentioned observables against model calculations is performed. Two codes are employed for the computation of the models: 1) the first one is the semi-analytic code where the energy balance equation is solved for a homologously expanding envelope of constant density (for details see Zampieri et al. 2003); 2) the other one is the new general-relativistic, radiation-hydrodynamics Lagrangian code presented in Pumo et al. (2010) and Pumo & Zampieri (2011), which is able to simulate the evolution of the physical properties of the CC-SN ejecta and the behavior of the main observables from the breakout of the shock wave at the stellar surface up to the nebular stage. The distinctive features of this new code are (cf. also Pumo & Zampieri 2013): a) an accurate treatment of radiative transfer coupled to hydrodynamics, b) a fully implicit Lagrangian approach to solve the coupled non-linear finite difference system of general-relativistic, radiation-hydrodynamics equations, and c) a description of the evolution of ejected material which takes into account both the gravitational effects of the compact remnant and the heating effects linked to the decay of the radioactive isotopes synthesized during the SN explosion.

The semi-analytic code used to carry out a preparatory study aimed at constraining the parameter space describing the SN progenitor at the explosion. The results of such study are exploited to guide the more realistic, but time consuming model calculations performed with the general-relativistic, radiation-hydrodynamics code.

We note that modelling with both codes is appropriate, since the emission of SN 2013ab is dominated by the expanding ejecta. However, in performing the χ^2 fit, we do not include the observational data taken at early phases (first $\sim 20\text{--}30$ days after explosion) because our model is not able to accurately reproduce the early evolution of the main observables, due to the approximate initial density profile used in the simulations which does not precisely reproduce the radial profile of the outermost high-velocity shell of the ejecta forming after the breakout of the shock wave at the stellar surface (cf. Pumo & Zampieri 2011).

The explosion epoch (JD = 2456340.0) and distance modulus ($\mu = 31.90$ mag) adopted in this paper (see § 3) are used to fix the explosion epoch and to compute the bolometric luminosity of SN 2013ab, both necessary to perform the comparison with model calculations. Since we do not have infrared (IR) observations for SN 2013ab, we computed true bolometric luminosity by adding IR contribution, assuming SN 2013ab has similar optical to IR flux ratio as observed for SN 1999em. Adopting a ^{56}Ni mass of $0.06 M_{\odot}$ (see § 4.4), the best fit procedure returns values of kinetic plus thermal energy of 0.35 foe , initial radius of $4.2 \times 10^{13} \text{ cm}$ ($\sim 600 R_{\odot}$) and envelope mass of $7 M_{\odot}$ (see Fig. 18), with an estimated uncertainty on the modelling parameters of about 15%. Adding the mass of the compact remnant ($\sim 1.5\text{--}2.0 M_{\odot}$) to that of the ejected material, the mass of the progenitor of SN 2013ab at the explosion would be $\sim 9 M_{\odot}$.

From the middle panel of Fig. 18 one can note a small (15–20%) discrepancy between the observed photospheric velocity and our best-fitting model. Such discrepancy may

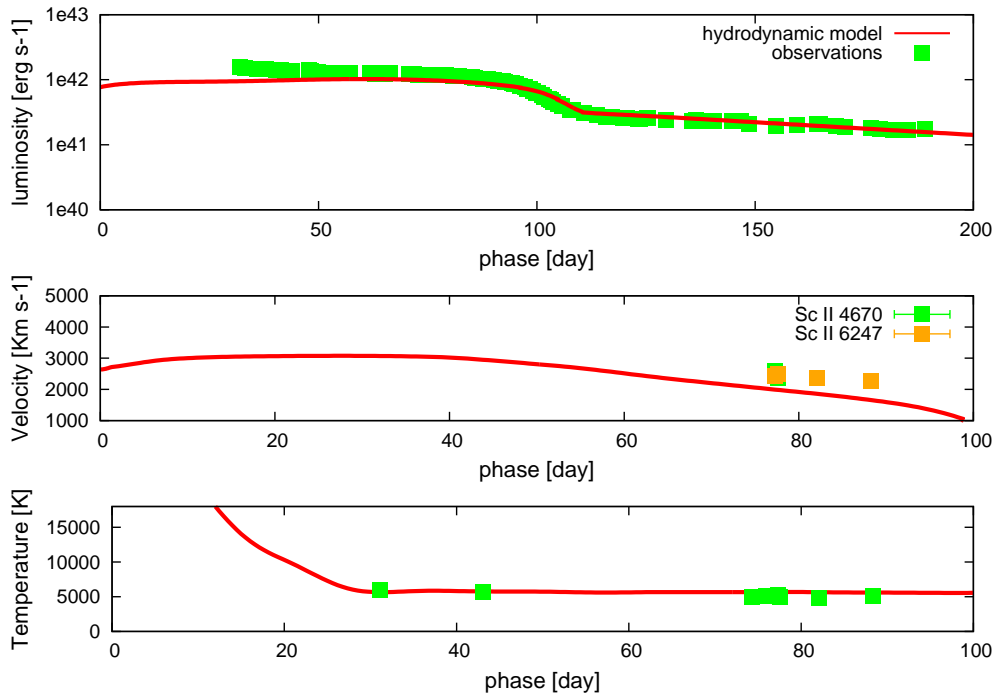


Figure 18. Comparison of the evolution of the main observables of SN 2013ab with the best-fit model computed using the general-relativistic, radiation-hydrodynamics code (total energy 0.35 foe, initial radius 4.2×10^{13} cm, envelope mass $7 M_{\odot}$). Top, middle, and bottom panels show the bolometric light curve, the photospheric velocity, and the photospheric temperature as a function of time. To better estimate the photosphere velocity from observations, we use the minima of the profile of the Sc II lines which are considered good tracer of the photosphere velocity in Type II SNe. As for the photospheric temperature, we use the blackbody temperature derived from the blackbody fits to the spectral continuum.

be linked to a systematic shift between the true photospheric velocity and the values estimated from the observed P-Cygni line profiles (Dessart & Hillier 2005a), according to which the optical depth in the lines could be higher than that in the continuum, causing a shift of the line photosphere to a larger radius (see also Inserra et al. 2013). Nevertheless we notice that the discrepancy can be eliminated by adopting for the model higher values for the initial radius ($\sim 6 \times 10^{13}$ cm), the energy (~ 0.6 foe) and the envelope mass (up to $13 M_{\odot}$). However in this case we get a worse fit to the observed light curve, with a longer (by about 30%) plateau.

The values reported above are consistent with a core collapse scenario from a typical red super-giant progenitor of relatively low mass. The radius estimate is also consistent within errors with that estimated from early photospheric temperatures described in §7.1.

8 SUMMARY

In this paper we present high-cadence broadband photometric and low resolution spectroscopic observations of SN 2013ab spanning a duration of about 6 months. In total, we collected 135 epoch of photometric and 25 epochs of spectroscopic observations. A brief summary of the results obtained in this work is given below.

(i) The light curve and the bolometric luminosity comparisons with other SNe IIP suggest that SN 2013ab is a normal SN IIP, though with a relatively large plateau decline rate (0.92 mag 100 d $^{-1}$ in the V band) and a shorter

plateau duration (~ 78 d). The ^{56}Ni mass estimated by comparing the tail luminosity with that of SN 1987A yields a value of $0.064 M_{\odot}$.

(ii) Spectroscopic comparisons show strong resemblance with canonical type IIP events. Earliest spectra show a featureless continuum. As the SN evolve, the spectra develop metal lines (calcium, iron, scandium, barium, titanium and neutral sodium). Nebular phase spectra show emission lines with little or no P-Cygni signatures. Spectra until 77d with good signal-to-noise ratio are modeled using SYNOW to identify most of the prominent features and to estimate expansion velocities for the He I , Fe II and $\text{H}\beta$ lines.

(iii) The EPM has been applied to SN 2013ab using the SYNOW-derived velocities and BVI photometric data. This provides an independent and reliable estimate of the distance of the galaxy NGC 5669 as 24.3 ± 1.0 Mpc.

(iv) We constrained the physical properties of SN 2013ab at the explosion by means of a hydrodynamical modelling of the main observables which uses the general-relativistic, radiation-hydrodynamics code described in Pumo & Zampieri (2011). The kinetic plus thermal energy is estimated to be ~ 0.35 foe, the progenitor mass is $\sim 9 M_{\odot}$ and the radius is about $600 R_{\odot}$.

ACKNOWLEDGMENTS

This work makes use of observations from the LCOGT network. We are thankful to the observing and technical staffs of LCOGT, ARIES, HCT and Asiago telescopes for their

kind cooperation in observation of SN 2013ab. We gratefully acknowledge the services of the NASA ADS and NED databases and also the online supernova spectrum archive (SUSPECT) which are used to access data and references in this paper. We acknowledge the TriGrid VL project and the INAF-Astronomical Observatory of Padua for the use of computer facilities. M.L.P. and A.P. acknowledges the financial support from CSFNSM and from the PRIN-INAF 2011 “Transient Universe: from ESO Large to PESSTO” (P.I. S. Benetti). We are also thankful to the anonymous referee, whose comments and suggestions has helped in significant improvement of the manuscript.

REFERENCES

Anderson J. P. et al., 2014a, MNRAS, 441, 671
 Anderson J. P. et al., 2014b, ApJ, 786, 67
 Arnett D., 1996, Supernovae and Nucleosynthesis: An Investigation of the History of Matter from the Big Bang to the Present
 Arnett W. D., 1980, ApJ, 237, 541
 Barbon R., Benetti S., Rosino L., Cappellaro E., Turatto M., 1990, A&A, 237, 79
 Bayless A. J. et al., 2013, ApJL, 764, L13
 Bersten M. C., Benvenuto O., Hamuy M., 2011, ApJ, 729, 61
 Blanchard P. et al., 2013, Central Bureau Electronic Telegrams, 3422, 1
 Bose S., Kumar B., 2014, ApJ, 782, 98
 Bose S. et al., 2013, MNRAS, 433, 1871
 Branch D. et al., 2002, ApJ, 566, 1005
 Breeveld A. A., Landsman W., Holland S. T., Roming P., Kuin N. P. M., Page M. J., 2011, in J.E. McEnery, J.L. Racusin, N. Gehrels, eds, American Institute of Physics Conference Series. American Institute of Physics Conference Series, Vol. 1358, pp. 373–376
 Brown P. J. et al., 2009, AJ, 137, 4517
 Brown T. M. et al., 2013, PASP, 125, 1031
 Chugai N. N., 1988, Soviet Astronomy Letters, 14, 334
 Dall’Ora M. et al., 2014, ApJ, 787, 139
 Dessart L., Hillier D. J., 2005a, A&A, 439, 671
 Dessart L., Hillier D. J., 2005b, A&A, 437, 667
 Dessart L., Hillier D. J., 2005c, in R. Humphreys, K. Stanek, eds, The Fate of the Most Massive Stars. Astronomical Society of the Pacific Conference Series, Vol. 332, p. 415
 Dessart L., Hillier D. J., 2006, A&A, 447, 691
 Dessart L. et al., 2008, ApJ, 675, 644
 Eastman R. G., Schmidt B. P., Kirshner R., 1996, ApJ, 466, 911
 Elmhamdi A., Chugai N. N., Danziger I. J., 2003a, A&A, 404, 1077
 Elmhamdi A. et al., 2003b, MNRAS, 338, 939
 Fassia A. et al., 2001, MNRAS, 325, 907
 Fisher A., Branch D., Nugent P., Baron E., 1997, ApJL, 481, L89
 Fisher A., Branch D., Hatano K., Baron E., 1999, MNRAS, 304, 67
 Hamuy M., 2003, ApJ, 582, 905
 Hamuy M., Suntzeff N. B., 1990, AJ, 99, 1146
 Hamuy M., Suntzeff N. B., Heathcote S. R., Walker A. R., Gigoux P., Phillips M. M., 1994, PASP, 106, 566
 Hamuy M. et al., 2001, ApJ, 558, 615
 Hamuy M. A., 2001, Ph.D. thesis, The University of Arizona
 Hanuschik R. W., Dachs J., 1987, A&A, 182, L29
 Heger A., Fryer C. L., Woosley S. E., Langer N., Hartmann D. H., 2003, ApJ, 591, 288
 Horne K., 1986, PASP, 98, 609
 Inserra C., Baron E., Turatto M., 2012a, MNRAS, 422, 1178
 Inserra C. et al., 2011, MNRAS, 417, 261
 Inserra C. et al., 2012b, MNRAS, 422, 1122
 Inserra C. et al., 2013, A&A, 555, A142
 Jones M. I. et al., 2009, ApJ, 696, 1176
 Kasen D., Woosley S. E., 2009, ApJ, 703, 2205
 Kirshner R. P., Kwan J., 1974, ApJ, 193, 27
 Landolt A. U., 2009, AJ, 137, 4186
 Leonard D. C. et al., 2002a, AJ, 124, 2490
 Leonard D. C. et al., 2002b, PASP, 114, 35
 Maguire K. et al., 2010, MNRAS, 404, 981
 Makarov D., Prugniel P., Terekhova N., Courtois H., Vaughn I., 2014, A&A, 570, A13
 Marion G. H. et al., 2014, ApJ, 781, 69
 Menzies J. W. et al., 1987, MNRAS, 227, 39P
 Milisavljevic D. et al., 2013, ApJ, 767, 71
 Oke J. B., 1990, AJ, 99, 1621
 Olivares E. F. et al., 2010, ApJ, 715, 833
 Pastorello A. et al., 2005, MNRAS, 360, 950
 Pastorello A. et al., 2009, MNRAS, 394, 2266
 Pastorello A. et al., 2012, A&A, 537, A141
 Pastorello A. et al., 2015, MNRAS, 449, 1921
 Patat F., Barbon R., Cappellaro E., Turatto M., 1994, A&A, 282, 731
 Poole T. S. et al., 2008, MNRAS, 383, 627
 Pumo M. L., Zampieri L., 2011, ApJ, 741, 41
 Pumo M. L., Zampieri L., 2013, MNRAS, 434, 3445
 Pumo M. L., Zampieri L., Turatto M., 2010, Memorie della Societa Astronomica Italiana Supplementi, 14, 123
 Pumo M. L. et al., 2009, ApJL, 705, L138
 Quimby R. M., Wheeler J. C., Höflich P., Akerlof C. W., Brown P. J., Rykoff E. S., 2007, ApJ, 666, 1093
 Rabinak I., Waxman E., 2011, ApJ, 728, 63
 Sagar R., Kumar B., Omar A., Joshi Y. C., 2012, in Astronomical Society of India Conference Series. Astronomical Society of India Conference Series, Vol. 4, p. 173
 Sahu D. K., Anupama G. C., Srividya S., Muneer S., 2006, MNRAS, 372, 1315
 Schlafly E. F., Finkbeiner D. P., 2011, ApJ, 737, 103
 Shivvers I., Mauerhan J. C., Leonard D. C., Filippenko A. V., Fox O. D., 2014, ArXiv e-prints
 Smartt S. J., Eldridge J. J., Crockett R. M., Maund J. R., 2009, MNRAS, 395, 1409
 Stetson P. B., 1987, PASP, 99, 191
 Takáts K., Vinkó J., 2012, MNRAS, 419, 2783
 Takáts K. et al., 2014, MNRAS, 438, 368
 Theureau G., Hanski M. O., Coudreau N., Hallet N., Martin J. M., 2007, A&A, 465, 71
 Tomasella L. et al., 2013, MNRAS, 434, 1636
 Tsvetkov D. Y., Goranskij V., Pavlyuk N., 2008, Peremenye Zvezdy, 28, 8

Tully R. B., Rizzi L., Shaya E. J., Courtois H. M., Makarov D. I., Jacobs B. A., 2009, AJ, 138, 323

Turatto M., Benetti S., Cappellaro E., 2003, in W. Hillebrandt, B. Leibundgut, eds, *From Twilight to Highlight: The Physics of Supernovae*. p. 200

Utrobin V. P., Chugai N. N., 2009, A&A, 506, 829

Valenti S. et al., 2015, MNRAS, 448, 2608

van Dokkum P. G., 2001, PASP, 113, 1420

Zampieri L., Pastorello A., Turatto M., Cappellaro E., Benetti S., Altavilla G., Mazzali P., Hamuy M., 2003, MNRAS, 338, 711

Zheng W., Blanchard P., Cenko S. B., Filippenko A. V., Cucchiara A., 2013, The Astronomer's Telegram, 4823, 1

APPENDIX A: PHOTOMETRY

Photometric images were bias subtracted and flat fielded, then cosmic ray removal were performed using standard tasks available in **IRAF**⁴. Due to the position of SN in its host galaxy, we performed PSF photometry on all frames using DAOPHOT⁵ routines. The measured SN flux was significantly affected by the host galaxy flux, therefore an annulus has been chosen conservatively to estimate the host galaxy background.

To calibrate the instrumental light curves of SN 2013ab in *UBVRI*, obtained from ARIES telescopes, four Landolt (2009) standard fields PG 1323, PG 1633, SA 104 and SA 107 were observed on 8 March, 2014 with 104-cm ST under good photometric sky condition with low atmospheric extinction and a typical image FWHM $\sim 1''.9$ in *V* band. Multiple standard fields at different airmasses were used to compute the zero points, colour coefficients as well as extinction for different filters. In total 27 standard stars were used for calibration having *V* magnitudes from 11.0 to 15.4. The root-mean-square scatter between standard and the re-calibrated magnitudes of these Landolt stars were found to be ~ 0.4 mag in *U*, ~ 0.2 mag in *B*, ~ 0.1 mag in *V, R* and ~ 0.3 mag in *I* band. We used the obtained coefficients to standardize 11 non-variable and isolated field stars in the SN frame, which are tabulated in Table. A1. These secondary standards allows us to calibrate the SN light curve obtained using differential photometry. Similarly to standardize the data collected from LCOGT in *BVgri* bands, several secondary standard in the SN field are selected, few of which are also listed in Table. A1. Since, *B* and *V* bands are in common to ARIES and LCOGT data, to have an uniformity we preferred to used LCOGT secondary standards for all *BV* bands data. *Swift*/UVOT data were analyzed following the methods described by Poole et al. (2008) and Brown et al. (2009) but adopting the revised zeropoints and sensitivity from Breeveld et al. (2011). Template images in all UVOT bands are obtained on 13 March, 2015 (755d), which are used to estimate background fluxes, using same aperture as

⁴ **IRAF** stands for Image Reduction and Analysis Facility distributed by the National Optical Astronomy Observatories which is operated by the Association of Universities for research in Astronomy, Inc. under co-operative agreement with the National Science Foundation.

⁵ DAOPHOT stands for Dominion Astrophysical Observatory Photometry (Stetson 1987).

used for SN measurement. These fluxes are subtracted from SN to eliminate flux contamination due to host galaxy. The final photometry in the *UBVRI*, *gri* and UVOT bands is tabulated in Table A2.

Table A1. Coordinates (α, δ) and calibrated magnitudes of secondary standard stars in the field of SN 2013ab. The quoted errors in magnitude include both photometric and calibration errors and it denote 1σ uncertainty.

Secondary standards used to calibrate <i>URI</i> data.					
α_{J2000} (h m s)	δ_{J2000} ($^{\circ}$ '')	<i>U</i> (mag)	<i>R</i> (mag)	<i>I</i> (mag)	
14:32:38	+9:56:39	17.654 \pm 0.085	15.452 \pm 0.016	14.967 \pm 0.014	
14:32:36	+9:56:00	17.406 \pm 0.028	16.134 \pm 0.017	15.744 \pm 0.016	
14:32:33	+9:54:45	16.968 \pm 0.022	15.851 \pm 0.017	15.440 \pm 0.016	
14:32:38	+9:52:24	17.709 \pm 0.034	16.034 \pm 0.020	15.550 \pm 0.021	
14:32:28	+9:49:43	19.362 \pm 0.204	15.628 \pm 0.015	14.616 \pm 0.015	
14:32:45	+9:48:37	18.118 \pm 0.062	16.549 \pm 0.017	16.109 \pm 0.020	
14:33:02	+9:54:41	18.789 \pm 0.097	15.133 \pm 0.013	14.096 \pm 0.015	
14:33:07	+9:55:52	17.354 \pm 0.023	16.085 \pm 0.013	15.649 \pm 0.013	
14:33:02	+9:56:03	17.828 \pm 0.031	16.422 \pm 0.012	15.996 \pm 0.014	
14:33:01	+9:57:25	14.520 \pm 0.011	13.770 \pm 0.009	13.418 \pm 0.013	
14:32:46	+9:56:10	17.918 \pm 0.071	16.882 \pm 0.013	16.469 \pm 0.015	

Secondary standards used to calibrate <i>BVgri</i> data.						
α_{J2000} (h m s)	δ_{J2000} ($^{\circ}$ '')	<i>B</i> (mag)	<i>V</i> (mag)	<i>g</i> (mag)	<i>r</i> (mag)	<i>i</i> (mag)
14:32:24	+9:52:12	18.947 \pm 0.098	18.518 \pm 0.032	18.749 \pm 0.019	18.336 \pm 0.022	18.241 \pm 0.026
14:32:26	+9:50:09	16.924 \pm 0.013	16.374 \pm 0.011	16.648 \pm 0.011	16.147 \pm 0.010	16.009 \pm 0.026
14:32:32	+9:47:16	17.557 \pm 0.040	16.977 \pm 0.025	17.321 \pm 0.025	16.788 \pm 0.016	16.629 \pm 0.021
14:32:32	+9:57:48	17.994 \pm 0.021	17.428 \pm 0.016	17.733 \pm 0.013	17.196 \pm 0.012	17.055 \pm 0.022
14:32:37	+9:58:48	18.937 \pm 0.048	17.948 \pm 0.023	18.461 \pm 0.019	17.413 \pm 0.013	16.961 \pm 0.013
14:32:40	+9:45:54	14.499 \pm 0.016	14.064 \pm 0.010	14.286 \pm 0.010	13.912 \pm 0.010	13.814 \pm 0.011
14:32:44	+9:54:24	16.593 \pm 0.012	15.759 \pm 0.010	16.166 \pm 0.011	15.426 \pm 0.016	15.203 \pm 0.023
14:32:48	+9:46:33	19.776 \pm 0.083	19.286 \pm 0.056	19.547 \pm 0.057	19.189 \pm 0.042	19.132 \pm 0.173
14:32:59	+9:45:23	17.241 \pm 0.021	16.804 \pm 0.013	17.022 \pm 0.013	16.635 \pm 0.012	16.497 \pm 0.013
14:33:02	+9:54:41	17.423 \pm 0.016	16.078 \pm 0.011	16.746 \pm 0.011	15.450 \pm 0.011	14.661 \pm 0.010
14:33:07	+9:55:52	17.096 \pm 0.014	16.462 \pm 0.012	16.746 \pm 0.011	16.216 \pm 0.011	16.033 \pm 0.011
14:33:11	+9:59:27	17.485 \pm 0.015	16.674 \pm 0.012	17.092 \pm 0.012	16.309 \pm 0.011	16.042 \pm 0.012
14:33:13	+9:49:03	16.591 \pm 0.012	16.059 \pm 0.011	16.329 \pm 0.011	15.865 \pm 0.011	15.725 \pm 0.011
14:33:14	+9:52:02	18.502 \pm 0.060	17.726 \pm 0.028	18.161 \pm 0.016	17.349 \pm 0.012	17.049 \pm 0.016
14:33:15	+9:51:37	15.060 \pm 0.012	14.534 \pm 0.010	14.776 \pm 0.010	14.344 \pm 0.010	14.230 \pm 0.011
14:33:18	+9:47:11	17.575 \pm 0.168	17.052 \pm 0.062	17.586 \pm 0.068	16.800 \pm 0.013	16.531 \pm 0.014

A1 Photometric data

Table A2: Photometric evolution of SN 2013ab. Errors denote 1σ uncertainty.

UT Date (yyyy/mm/dd)	JD 2456000+	Phase ^a (day)	<i>U</i> (mag)	<i>B</i> (mag)	<i>V</i> (mag)	<i>R</i> (mag)	<i>I</i> (mag)	<i>g</i> (mag)	<i>r</i> (mag)	<i>i</i> (mag)	Tel ^b /Inst
2013-02-15.50	339.00	-1.00	—	—	—	—	—	—	>18.500	—	6
2013-02-17.50	341.00	1.00	—	—	—	—	—	—	17.600 \pm 0.095	—	6
2013-02-19.20	342.70	2.70	—	—	—	—	—	—	15.093 \pm 0.095	—	5
2013-02-20.29	343.79	3.79	—	—	—	—	—	15.007 \pm 0.022	15.094 \pm 0.047	15.297 \pm 0.010	2,5
2013-02-20.93	344.43	4.43	14.231 \pm 0.040	—	—	14.873 \pm 0.015	14.767 \pm 0.030	—	—	—	1
2013-02-21.34	344.84	4.84	—	14.812 \pm 0.015	14.779 \pm 0.012	—	—	14.805 \pm 0.018	14.874 \pm 0.011	14.956 \pm 0.017	5
2013-02-21.57	345.07	5.07	—	—	—	—	—	14.964 \pm 0.016	14.767 \pm 0.068	14.994 \pm 0.064	3
2013-02-22.34	345.84	5.84	—	14.813 \pm 0.015	14.747 \pm 0.018	—	—	14.825 \pm 0.018	14.759 \pm 0.017	14.855 \pm 0.013	5
2013-02-22.90	346.40	6.40	14.173 \pm 0.040	14.804 \pm 0.025	—	14.730 \pm 0.014	14.586 \pm 0.029	—	—	—	1
2013-02-23.34	346.84	6.84	—	14.793 \pm 0.013	14.705 \pm 0.023	—	—	14.734 \pm 0.028	14.744 \pm 0.037	14.740 \pm 0.030	5
2013-02-24.34	347.84	7.84	—	14.793 \pm 0.014	—	—	—	14.761 \pm 0.013	14.699 \pm 0.010	14.763 \pm 0.012	5
2013-02-24.80	348.30	8.30	14.231 \pm 0.041	14.868 \pm 0.025	—	14.677 \pm 0.014	14.517 \pm 0.030	—	—	—	1
2013-02-25.34	348.84	8.84	—	14.838 \pm 0.015	14.691 \pm 0.019	—	—	14.776 \pm 0.013	14.721 \pm 0.025	14.776 \pm 0.016	5
2013-02-26.34	349.84	9.84	—	14.871 \pm 0.011	14.729 \pm 0.021	—	—	14.751 \pm 0.020	14.717 \pm 0.021	14.786 \pm 0.009	5
2013-02-26.90	350.40	10.40	14.342 \pm 0.041	14.885 \pm 0.025	—	14.698 \pm 0.014	14.552 \pm 0.030	—	—	—	1
2013-02-27.34	350.84	10.84	—	14.880 \pm 0.014	14.783 \pm 0.011	—	—	14.903 \pm 0.013	14.685 \pm 0.022	14.871 \pm 0.021	5
2013-02-27.80	351.30	11.30	14.402 \pm 0.041	14.916 \pm 0.025	—	14.712 \pm 0.014	14.580 \pm 0.029	—	—	—	1
2013-02-28.34	351.84	11.84	—	14.860 \pm 0.015	14.814 \pm 0.018	—	—	14.831 \pm 0.016	14.741 \pm 0.014	14.822 \pm 0.015	5
2013-02-28.86	352.36	12.36	14.497 \pm 0.040	14.974 \pm 0.025	—	14.733 \pm 0.014	14.612 \pm 0.029	—	—	—	1
2013-03-01.44	352.94	12.94	—	15.018 \pm 0.005	14.901 \pm 0.006	—	—	14.935 \pm 0.005	14.809 \pm 0.005	14.911 \pm 0.009	5
2013-03-02.44	353.94	13.94	—	14.950 \pm 0.006	14.889 \pm 0.010	—	—	14.925 \pm 0.007	14.777 \pm 0.009	14.934 \pm 0.009	5
2013-03-03.39	354.89	14.89	—	15.092 \pm 0.017	14.826 \pm 0.018	—	—	14.917 \pm 0.003	14.798 \pm 0.006	14.951 \pm 0.007	5
2013-03-04.44	355.94	15.94	—	15.046 \pm 0.005	14.920 \pm 0.005	—	—	14.957 \pm 0.005	14.802 \pm 0.005	14.945 \pm 0.009	5
2013-03-04.84	356.34	16.34	14.715 \pm 0.040	15.073 \pm 0.025	—	14.770 \pm 0.014	14.668 \pm 0.029	—	—	—	1
2013-03-05.32	356.82	16.82	—	15.102 \pm 0.023	14.885 \pm 0.018	—	—	14.972 \pm 0.015	14.753 \pm 0.024	14.893 \pm 0.027	5
2013-03-06.32	357.82	17.82	—	15.122 \pm 0.012	14.905 \pm 0.021	—	—	15.007 \pm 0.019	14.750 \pm 0.026	14.930 \pm 0.023	5
2013-03-06.85	358.35	18.35	14.879 \pm 0.040	15.124 \pm 0.025	—	14.768 \pm 0.014	14.652 \pm 0.029	—	—	—	1
2013-03-07.82	359.32	19.32	14.951 \pm 0.040	15.162 \pm 0.025	—	14.762 \pm 0.014	14.642 \pm 0.029	—	—	—	1
2013-03-08.31	359.81	19.81	—	15.198 \pm 0.017	—	—	—	—	—	—	5
2013-03-09.36	360.86	20.86	—	15.196 \pm 0.016	14.886 \pm 0.012	—	—	15.026 \pm 0.009	14.783 \pm 0.009	—	5
2013-03-10.35	361.85	21.85	—	15.254 \pm 0.016	14.935 \pm 0.026	—	—	15.075 \pm 0.012	14.832 \pm 0.013	14.934 \pm 0.015	5
2013-03-11.33	362.83	22.83	—	15.236 \pm 0.010	14.963 \pm 0.014	—	—	15.067 \pm 0.016	14.814 \pm 0.019	14.939 \pm 0.021	5
2013-03-12.37	363.87	23.87	—	15.363 \pm 0.016	14.952 \pm 0.019	—	—	15.091 \pm 0.014	14.827 \pm 0.004	14.923 \pm 0.004	5
2013-03-12.80	364.30	24.30	15.503 \pm 0.041	15.354 \pm 0.025	14.994 \pm 0.012	14.756 \pm 0.014	14.605 \pm 0.029	—	—	—	1
2013-03-14.44	365.94	25.94	—	15.422 \pm 0.012	15.036 \pm 0.013	—	—	15.202 \pm 0.011	14.890 \pm 0.015	14.985 \pm 0.018	5
2013-03-15.88	367.38	27.38	15.819 \pm 0.042	15.486 \pm 0.025	15.056 \pm 0.012	14.793 \pm 0.014	14.636 \pm 0.029	—	—	—	1
2013-03-19.94	371.44	31.44	16.145 \pm 0.044	15.665 \pm 0.025	15.166 \pm 0.012	14.867 \pm 0.014	14.693 \pm 0.029	—	—	—	1
2013-03-20.44	371.94	31.94	—	15.695 \pm 0.007	15.113 \pm 0.005	—	—	15.383 \pm 0.003	14.934 \pm 0.004	15.035 \pm 0.007	5
2013-03-21.71	373.21	33.21	16.243 \pm 0.053	—	15.203 \pm 0.013	14.900 \pm 0.015	14.692 \pm 0.031	—	—	—	1
2013-03-24.43	375.93	35.93	—	15.812 \pm 0.010	15.230 \pm 0.007	—	—	15.464 \pm 0.005	15.003 \pm 0.005	—	5
2013-03-24.90	376.40	36.40	—	15.848 \pm 0.027	15.248 \pm 0.013	14.927 \pm 0.014	—	—	—	—	1
2013-03-25.75	377.25	37.25	16.633 \pm 0.059	15.866 \pm 0.027	15.257 \pm 0.009	14.936 \pm 0.015	14.718 \pm 0.030	—	—	—	1
2013-03-26.38	377.88	37.88	—	15.911 \pm 0.012	15.245 \pm 0.012	—	—	—	—	—	5
2013-03-28.81	380.31	40.31	16.681 \pm 0.062	15.968 \pm 0.028	15.282 \pm 0.013	14.966 \pm 0.015	14.729 \pm 0.030	—	—	—	1
2013-03-29.78	381.28	41.28	16.814 \pm 0.104	15.982 \pm 0.029	15.303 \pm 0.013	14.971 \pm 0.014	14.722 \pm 0.030	—	—	—	1
2013-03-30.87	382.37	42.37	16.910 \pm 0.066	16.035 \pm 0.027	15.316 \pm 0.013	14.997 \pm 0.015	14.763 \pm 0.029	—	—	—	1
2013-04-01.38	383.88	43.88	—	16.068 \pm 0.013	15.278 \pm 0.014	—	—	15.619 \pm 0.014	15.073 \pm 0.017	15.083 \pm 0.018	5
2013-04-05.39	387.89	47.89	—	16.073 \pm 0.204	15.277 \pm 0.025	—	—	15.640 \pm 0.020	15.064 \pm 0.026	15.074 \pm 0.028	5
2013-04-05.83	388.33	48.33	17.143 \pm 0.055	16.074 \pm 0.026	15.307 \pm 0.012	14.986 \pm 0.014	14.736 \pm 0.029	—	—	—	1
2013-04-06.40	388.90	48.90	—	16.183 \pm 0.030	—	—	—	—	—	—	5
2013-04-06.85	389.35	49.35	17.200 \pm 0.042	16.087 \pm 0.018	15.317 \pm 0.008	15.117 \pm 0.010	14.731 \pm 0.021	—	—	—	1
2013-04-07.39	389.89	49.89	—	16.203 \pm 0.010	15.340 \pm 0.012	—	—	15.693 \pm 0.013	15.110 \pm 0.014	15.119 \pm 0.012	5
2013-04-10.88	393.38	53.38	17.429 \pm 0.047	16.243 \pm 0.026	15.381 \pm 0.012	15.032 \pm 0.014	14.751 \pm 0.029	—	—	—	1
2013-04-11.85	394.35	54.35	17.487 \pm 0.073	16.243 \pm 0.026	15.383 \pm 0.012	15.030 \pm 0.014	14.748 \pm 0.029	—	—	—	1
2013-04-14.36	396.86	56.86	—	16.362 \pm 0.011	15.372 \pm 0.010	—	—	15.771 \pm 0.008	15.167 \pm 0.008	15.194 \pm 0.009	5
2013-04-14.77	397.27	57.27	17.522 \pm 0.052	16.288 \pm 0.026	15.403 \pm 0.012	15.042 \pm 0.014	14.761 \pm 0.029	—	—	—	1

UT Date (yyyy/mm/dd)	JD 2456000+	Phase ^a (day)	<i>U</i> (mag)	<i>B</i> (mag)	<i>V</i> (mag)	<i>R</i> (mag)	<i>I</i> (mag)	<i>g</i> (mag)	<i>r</i> (mag)	<i>i</i> (mag)	Tel ^b /Inst
2013-04-19.32	401.82	61.82	—	16.402 ± 0.014	15.373 ± 0.011	—	—	15.838 ± 0.007	15.197 ± 0.010	15.122 ± 0.013	5
2013-04-20.32	402.82	62.82	—	16.390 ± 0.012	15.420 ± 0.010	—	—	15.804 ± 0.006	15.229 ± 0.009	15.191 ± 0.012	5
2013-04-21.32	403.82	63.82	—	16.444 ± 0.018	15.387 ± 0.014	—	—	15.793 ± 0.013	15.153 ± 0.018	15.150 ± 0.016	5
2013-04-22.77	405.27	65.27	17.637 ± 0.098	16.415 ± 0.022	15.430 ± 0.009	15.061 ± 0.016	14.787 ± 0.030	—	—	—	1
2013-04-23.32	405.82	65.82	—	16.330 ± 0.026	15.411 ± 0.012	—	—	15.820 ± 0.014	15.182 ± 0.019	15.143 ± 0.017	5
2013-04-23.80	406.30	66.30	—	—	15.422 ± 0.017	15.084 ± 0.015	14.781 ± 0.030	—	—	—	1
2013-04-26.28	408.78	68.78	—	—	—	—	—	15.874 ± 0.018	15.099 ± 0.016	—	5
2013-04-28.28	410.78	70.78	—	16.480 ± 0.019	15.406 ± 0.014	—	—	15.818 ± 0.011	15.129 ± 0.016	15.137 ± 0.016	5
2013-04-29.28	411.78	71.78	—	16.520 ± 0.014	15.437 ± 0.011	—	—	15.858 ± 0.009	15.187 ± 0.008	15.175 ± 0.012	5
2013-04-30.28	412.78	72.78	—	16.557 ± 0.013	15.486 ± 0.012	—	—	15.889 ± 0.011	15.227 ± 0.010	15.246 ± 0.013	5
2013-05-01.77	414.27	74.27	17.740 ± 0.053	—	15.444 ± 0.013	15.086 ± 0.014	14.792 ± 0.030	—	—	—	1
2013-05-03.27	415.77	75.77	—	16.617 ± 0.025	15.498 ± 0.015	—	—	15.885 ± 0.011	15.231 ± 0.012	—	5
2013-05-05.75	418.25	78.25	17.841 ± 0.094	—	15.466 ± 0.012	15.107 ± 0.014	14.820 ± 0.021	—	—	—	1
2013-05-06.76	419.26	79.26	17.920 ± 0.086	—	15.457 ± 0.012	15.094 ± 0.014	14.802 ± 0.029	—	—	—	1
2013-05-08.27	420.77	80.77	—	16.620 ± 0.027	15.562 ± 0.019	—	—	15.985 ± 0.015	15.298 ± 0.013	15.224 ± 0.021	5
2013-05-08.79	421.29	81.29	18.113 ± 0.061	—	15.494 ± 0.012	15.123 ± 0.015	14.815 ± 0.030	—	—	—	1
2013-05-09.72	422.22	82.22	18.070 ± 0.057	—	15.510 ± 0.009	15.119 ± 0.015	14.823 ± 0.030	—	—	—	1
2013-05-12.74	425.24	85.24	18.069 ± 0.078	—	15.567 ± 0.013	15.174 ± 0.015	14.815 ± 0.032	—	—	—	1
2013-05-13.24	425.74	85.74	—	16.793 ± 0.023	15.621 ± 0.015	—	—	16.084 ± 0.010	15.360 ± 0.011	15.329 ± 0.014	5
2013-05-15.24	427.74	87.74	—	16.874 ± 0.021	15.653 ± 0.014	—	—	16.127 ± 0.010	15.360 ± 0.009	15.349 ± 0.013	5
2013-05-16.26	428.76	88.76	—	16.827 ± 0.021	15.597 ± 0.013	—	—	16.093 ± 0.015	15.337 ± 0.012	—	5
2013-05-17.74	430.24	90.24	18.634 ± 0.147	—	15.668 ± 0.013	15.223 ± 0.014	14.926 ± 0.030	—	—	—	1
2013-05-18.71	431.21	91.21	—	—	15.718 ± 0.010	15.279 ± 0.015	14.969 ± 0.031	—	—	—	1
2013-05-19.69	432.19	92.19	—	—	15.740 ± 0.015	15.298 ± 0.016	14.978 ± 0.031	—	—	—	1
2013-05-20.26	432.76	92.76	—	17.002 ± 0.021	15.764 ± 0.015	—	—	16.256 ± 0.021	15.474 ± 0.027	15.425 ± 0.025	5
2013-05-21.72	434.22	94.22	—	—	15.783 ± 0.015	15.350 ± 0.012	15.025 ± 0.034	—	—	—	1
2013-05-22.23	434.73	94.73	—	17.154 ± 0.034	15.864 ± 0.014	—	—	16.382 ± 0.013	15.523 ± 0.016	15.466 ± 0.020	5
2013-05-22.72	435.22	95.22	—	17.002 ± 0.030	15.850 ± 0.011	15.390 ± 0.012	15.048 ± 0.023	—	—	—	1
2013-05-23.73	436.23	96.23	—	17.075 ± 0.047	15.950 ± 0.022	15.456 ± 0.019	15.129 ± 0.034	—	—	—	1
2013-05-24.74	437.24	97.24	—	17.191 ± 0.062	16.017 ± 0.022	15.543 ± 0.020	15.204 ± 0.037	—	—	—	1
2013-05-25.23	437.73	97.73	—	17.383 ± 0.125	16.092 ± 0.044	—	—	16.621 ± 0.052	15.738 ± 0.047	15.605 ± 0.033	5
2013-05-25.83	438.33	98.33	—	17.213 ± 0.089	16.081 ± 0.032	15.613 ± 0.021	15.270 ± 0.036	—	—	—	1
2013-05-26.72	439.22	99.22	—	17.417 ± 0.040	16.191 ± 0.015	15.677 ± 0.017	15.293 ± 0.033	—	—	—	1
2013-05-27.23	439.73	99.73	—	17.671 ± 0.021	16.264 ± 0.011	—	—	16.816 ± 0.008	15.842 ± 0.010	15.749 ± 0.010	5
2013-05-27.70	440.20	100.20	18.856 ± 0.355	17.505 ± 0.037	16.254 ± 0.014	15.729 ± 0.017	15.335 ± 0.032	—	—	—	1
2013-05-28.76	441.26	101.26	18.513 ± 0.293	17.638 ± 0.038	16.382 ± 0.014	15.829 ± 0.019	15.417 ± 0.033	—	—	—	1
2013-05-29.23	441.73	101.73	—	17.841 ± 0.024	16.517 ± 0.029	—	—	17.030 ± 0.011	16.018 ± 0.008	15.922 ± 0.014	5
2013-05-30.23	442.73	102.73	—	18.019 ± 0.021	16.605 ± 0.014	—	—	17.199 ± 0.014	16.128 ± 0.011	16.017 ± 0.010	5
2013-05-30.80	443.30	103.30	—	17.844 ± 0.038	16.594 ± 0.015	16.004 ± 0.017	—	—	—	—	1
2013-05-31.24	443.74	103.74	—	18.170 ± 0.039	16.736 ± 0.020	—	—	17.345 ± 0.015	16.241 ± 0.013	—	5
2013-06-01.23	444.73	104.73	—	18.259 ± 0.025	16.800 ± 0.018	—	—	17.422 ± 0.012	16.289 ± 0.010	16.204 ± 0.020	5
2013-06-02.23	445.73	105.73	—	18.485 ± 0.051	16.894 ± 0.027	—	—	17.548 ± 0.018	16.370 ± 0.015	16.256 ± 0.023	5
2013-06-04.18	447.68	107.68	—	18.599 ± 0.046	17.113 ± 0.023	—	—	17.734 ± 0.021	16.529 ± 0.017	16.411 ± 0.022	5
2013-06-04.78	448.28	108.28	—	—	17.048 ± 0.020	16.399 ± 0.022	—	—	—	—	1
2013-06-07.18	450.68	110.68	—	18.700 ± 0.047	17.207 ± 0.029	—	—	17.888 ± 0.022	16.744 ± 0.018	16.619 ± 0.026	5
2013-06-10.22	453.72	113.72	—	18.806 ± 0.084	17.278 ± 0.031	—	—	17.962 ± 0.025	16.715 ± 0.026	16.691 ± 0.036	5
2013-06-12.22	455.72	115.72	—	—	17.316 ± 0.028	—	—	18.003 ± 0.024	16.794 ± 0.021	16.651 ± 0.030	5
2013-06-12.68	456.18	116.18	19.743 ± 0.527	—	17.291 ± 0.031	16.632 ± 0.025	16.146 ± 0.037	—	—	—	1
2013-06-13.72	457.22	117.22	19.625 ± 0.411	—	17.293 ± 0.023	16.627 ± 0.024	16.161 ± 0.036	—	—	—	1
2013-06-16.13	459.63	119.63	—	18.911 ± 0.044	17.414 ± 0.018	—	—	18.053 ± 0.042	16.806 ± 0.017	16.727 ± 0.024	5
2013-06-17.20	460.70	120.70	—	18.885 ± 0.038	17.362 ± 0.110	—	—	—	—	—	5
2013-06-19.72	463.22	123.22	—	—	17.446 ± 0.036	16.749 ± 0.026	16.292 ± 0.038	—	—	—	1
2013-06-20.10	463.60	123.60	—	—	17.478 ± 0.026	—	—	18.052 ± 0.020	—	—	5
2013-06-21.73	465.23	125.23	—	—	17.463 ± 0.053	16.700 ± 0.034	16.245 ± 0.045	—	—	—	1
2013-06-22.05	465.55	125.55	—	18.790 ± 0.065	17.454 ± 0.021	—	—	18.007 ± 0.021	16.851 ± 0.012	16.794 ± 0.022	5
2013-06-24.05	467.55	127.55	—	19.004 ± 0.086	—	—	—	18.032 ± 0.018	16.901 ± 0.013	16.770 ± 0.015	5
2013-06-26.05	469.55	129.55	—	18.950 ± 0.048	17.519 ± 0.018	—	—	18.091 ± 0.015	16.896 ± 0.011	16.851 ± 0.015	5
2013-07-02.06	475.56	135.56	—	18.963 ± 0.029	17.623 ± 0.018	—	—	18.190 ± 0.014	16.912 ± 0.012	16.898 ± 0.013	5
2013-07-03.06	476.56	136.56	—	18.936 ± 0.032	17.533 ± 0.021	—	—	—	16.880 ± 0.017	16.911 ± 0.024	5

UT Date (yyyy/mm/dd)	JD 2456000+	Phase ^a (day)	<i>U</i> (mag)	<i>B</i> (mag)	<i>V</i> (mag)	<i>R</i> (mag)	<i>I</i> (mag)	<i>g</i> (mag)	<i>r</i> (mag)	<i>i</i> (mag)	Tel ^b /Inst
2013-07-04.21	477.71	137.71	—	18.933	—	—	—	—	—	16.990 ± 0.022	5
2013-07-05.21	478.71	138.71	—	19.027 ± 0.052	17.588 ± 0.020	—	—	18.178 ± 0.024	16.956 ± 0.011	16.937 ± 0.014	5
2013-07-06.21	479.71	139.71	—	18.875 ± 0.052	17.579 ± 0.026	—	—	18.168 ± 0.020	16.983 ± 0.015	16.965 ± 0.021	5
2013-07-07.19	480.69	140.69	—	18.936 ± 0.068	17.624 ± 0.035	—	—	18.188 ± 0.022	16.952 ± 0.020	16.952 ± 0.017	5
2013-07-11.15	484.65	144.65	—	18.865 ± 0.050	17.611 ± 0.024	—	—	18.185 ± 0.019	16.968 ± 0.017	17.067 ± 0.020	5
2013-07-13.15	486.65	146.65	—	18.910 ± 0.050	17.604 ± 0.028	—	—	18.206 ± 0.016	16.993 ± 0.014	17.026 ± 0.019	5
2013-07-15.18	488.68	148.68	—	—	17.773 ± 0.066	—	—	18.258 ± 0.078	17.089 ± 0.045	—	5
2013-07-21.18	494.68	154.68	—	19.072 ± 0.111	17.914 ± 0.043	—	—	18.240 ± 0.034	17.047 ± 0.021	17.215 ± 0.024	5
2013-07-26.18	499.68	159.68	—	19.058 ± 0.053	17.814 ± 0.035	—	—	18.260 ± 0.032	17.073 ± 0.018	17.197 ± 0.029	5
2013-07-30.72	504.22	164.22	—	19.044 ± 0.038	17.753 ± 0.021	—	—	—	—	—	5
2013-07-31.43	504.93	164.93	—	19.090 ± 0.111	17.708 ± 0.044	—	—	—	17.096 ± 0.027	17.257 ± 0.046	3
2013-08-01.17	505.67	165.67	—	19.070 ± 0.150	—	—	—	18.384 ± 0.030	—	—	5
2013-08-04.12	508.62	168.62	—	19.039 ± 0.113	17.900 ± 0.044	—	—	18.350 ± 0.025	17.129 ± 0.017	17.285 ± 0.025	5
2013-08-06.18	510.68	170.68	—	19.047 ± 0.068	17.886 ± 0.031	—	—	18.392 ± 0.024	17.247 ± 0.037	17.413 ± 0.035	5
2013-08-11.97	516.47	176.47	—	19.073 ± 0.125	18.005 ± 0.049	—	—	—	17.186 ± 0.022	17.385 ± 0.036	5
2013-08-14.01	518.51	178.51	—	19.074 ± 0.080	18.035 ± 0.036	—	—	18.487 ± 0.028	17.231 ± 0.017	17.422 ± 0.035	5
2013-08-16.99	521.49	181.49	—	—	18.099 ± 0.051	—	—	18.563 ± 0.036	—	17.428 ± 0.035	5
2013-08-20.15	524.65	184.65	—	—	—	—	—	18.613 ± 0.125	17.227 ± 0.041	17.433 ± 0.072	5
2013-08-20.42	524.92	184.92	—	19.089 ± 0.122	18.078 ± 0.051	—	—	—	—	—	5
2013-08-24.38	528.88	188.88	—	—	18.002 ± 0.060	—	—	—	—	—	3
2013-08-25.36	529.86	189.86	—	—	—	—	—	—	17.267 ± 0.036	17.526 ± 0.071	3

Swift UVOT photometry

UT Date (yyyy/mm/dd)	JD 2456000+	Phase ^a (day)	<i>uvw1</i> (mag)	<i>uvw2</i> (mag)	<i>uvm2</i> (mag)	<i>uvu</i> (mag)	<i>uvb</i> (mag)	<i>uvv</i> (mag)	Tel ^b /Inst
2013-02-21.18	344.68	4.68	13.404 ± 0.038	13.434 ± 0.042	13.301 ± 0.036	—	—	—	4
2013-02-21.94	345.44	5.44	13.486 ± 0.039	13.589 ± 0.052	13.442 ± 0.047	13.670 ± 0.052	15.010 ± 0.049	15.094 ± 0.056	4
2013-02-22.08	345.58	5.58	13.489 ± 0.037	13.629 ± 0.044	—	—	—	—	4
2013-02-22.51	346.01	6.01	13.616 ± 0.056	13.747 ± 0.071	—	—	—	—	4
2013-02-24.04	347.54	7.54	13.734 ± 0.035	14.133 ± 0.041	13.830 ± 0.035	—	—	—	4
2013-02-24.90	348.40	8.40	13.848 ± 0.043	14.363 ± 0.052	14.007 ± 0.037	13.819 ± 0.050	15.010 ± 0.046	14.962 ± 0.047	4
2013-02-24.98	348.48	8.48	—	—	14.083 ± 0.059	—	—	—	4
2013-02-27.30	350.80	10.80	—	14.895 ± 0.072	—	—	—	—	4
2013-02-27.98	351.48	11.48	14.395 ± 0.058	14.992 ± 0.072	14.742 ± 0.060	13.997 ± 0.051	15.072 ± 0.047	15.018 ± 0.049	4
2013-03-03.09	354.59	14.59	15.084 ± 0.060	15.792 ± 0.075	15.662 ± 0.063	14.340 ± 0.052	15.237 ± 0.047	15.132 ± 0.050	4
2013-03-06.13	357.63	17.63	15.635 ± 0.063	16.577 ± 0.082	16.574 ± 0.072	14.608 ± 0.052	15.258 ± 0.047	15.165 ± 0.049	4
2013-03-14.17	365.67	25.67	17.408 ± 0.116	18.759 ± 0.261	18.859 ± 0.320	15.680 ± 0.068	15.552 ± 0.054	15.220 ± 0.061	4
2013-03-18.21	369.71	29.71	17.710 ± 0.127	19.461 ± 0.364	19.231 ± 0.335	16.203 ± 0.066	15.739 ± 0.049	15.303 ± 0.051	4
2013-03-20.97	372.47	32.47	18.073 ± 0.153	19.120 ± 0.264	19.430 ± 0.385	16.458 ± 0.068	15.896 ± 0.049	15.354 ± 0.049	4
2013-03-27.97	379.47	39.47	18.913 ± 0.299	19.516 ± 0.549	—	17.096 ± 0.095	16.161 ± 0.054	—	4
2013-04-01.39	383.89	43.89	18.754 ± 0.266	19.548 ± 0.390	19.785 ± 0.538	17.276 ± 0.101	16.195 ± 0.053	15.439 ± 0.053	4
2013-04-05.20	387.70	47.70	18.935 ± 0.294	21.232 ± 1.634	19.854 ± 0.556	17.431 ± 0.105	16.391 ± 0.054	15.565 ± 0.053	4
2013-04-10.84	393.34	53.34	19.158 ± 0.359	20.750 ± 1.075	20.042 ± 0.671	17.637 ± 0.120	16.472 ± 0.055	15.548 ± 0.053	4
2013-04-21.92	404.42	64.42	19.450 ± 0.628	—	—	—	—	—	4
2013-04-26.01	408.51	68.51	19.505 ± 0.487	—	20.392 ± 1.262	17.890 ± 0.167	16.646 ± 0.087	15.615 ± 0.086	4
2013-05-01.32	413.82	73.82	20.646 ± 1.300	20.560 ± 0.882	20.642 ± 1.126	18.092 ± 0.160	16.728 ± 0.058	15.632 ± 0.054	4
2013-05-14.26	426.76	86.76	21.116 ± 2.278	20.650 ± 1.277	—	18.971 ± 0.456	16.825 ± 0.080	15.821 ± 0.080	4
2013-05-16.00	429.50	89.50	—	—	20.689 ± 1.217	18.496 ± 0.233	16.925 ± 0.066	15.858 ± 0.062	4
2013-05-20.95	433.45	93.45	20.929 ± 1.738	21.652 ± 2.536	20.850 ± 1.421	18.708 ± 0.279	17.223 ± 0.074	16.050 ± 0.067	4
2013-05-30.95	443.45	103.45	20.721 ± 1.389	21.184 ± 1.547	21.605 ± 2.708	19.429 ± 0.464	18.155 ± 0.115	16.923 ± 0.096	4

^a with reference to the explosion epoch JD 2456340.0^b 1: 104-cm Sampurnanand Telescope (ST) and 130-cm Devasthal fast optical telescope (DFOT), ARIES, India; 2: Faulkes Telescope South; 3: Faulkes Telescope North; 4: *Swift* UVOT data;

5: 1-m class telescopes of Las Cumbres Observatory Global Telescope (LCOGT) network; 6: IAU circular report.

APPENDIX B: SPECTROSCOPY

Spectroscopic data were reduced in the `IRAF` environment. All frames are corrected by bias subtraction and flat fielding. Cosmic ray rejection on each frame was done using Laplacian kernel detection algorithm for spectra (`L.A.Cosmic`; van Dokkum 2001). One-dimensional spectra were extracted using `apall` task which is based on optimal extraction algorithm by Horne (1986). Wavelength calibration was performed with the help of the `identify` task by using the arc spectra obtained for all telescopes during each night. The position of O I emission skyline at 5577Å was used to check the wavelength calibration and deviations were found to lie between 0.3 to 5.5Å, and this was corrected by applying a linear shift in wavelength.

The flux calibration of wavelength-calibrated spectra was done using `standard`, `sensfunc` and `calibrate` tasks. We used spectrophotometric standard fluxes from Oke (1990); Hamuy et al. (1994). All spectra were tied to an absolute flux scale using zeropoints determined from *UBVRI* magnitudes. To tie the spectra with photometry, individual spectrum was multiplied by wavelength dependent polynomial function and its *BVRI* filter-response convolved fluxes were compared with photometric fluxes at corresponding epoch. The multiplied polynomial was tuned to minimize the flux difference and obtain the tied spectrum. The one-dimensional spectra were corrected for heliocentric velocity of the host galaxy (1374 km s⁻¹; see §1) using `dopcor` tasks.

Table B1. Journal of spectroscopic observations of SN 2013ab. The spectral observations are made at 25 phases from 2 to 184d.

UT Date (yyyy-mm-dd.dd)	JD 2456000+	Phase ^a (days)	Telescope ^c	Range ^b μm	Exposure (s)
2013-02-18.70	342.20	2.20	FTS	0.32-1.00	1500
2013-02-19.74	343.24	3.24	FTS	0.32-1.00	1500
2013-02-24.71	348.21	8.21	FTS	0.32-1.00	1500
2013-02-28.59	352.09	12.09	FTN	0.32-1.00	1800
2013-03-01.08	352.58	12.58	PEN	0.00-0.00	1800
2013-03-01.50	353.00	13.00	FTN	0.32-1.00	1800
2013-03-02.51	354.01	14.01	FTN	0.32-1.00	1800
2013-03-03.51	355.01	15.01	FTN	0.32-1.00	1800
2013-03-04.59	356.09	16.09	FTN	0.32-1.00	1800
2013-03-06.71	358.21	18.21	FTS	0.32-1.00	2000
2013-03-17.93	369.43	29.43	HCT	0.38-0.84	1800
2013-03-19.63	371.13	31.13	FTS	0.32-1.00	2000
2013-03-31.58	383.08	43.08	FTS	0.32-1.00	2400
2013-05-01.84	414.34	74.34	HCT	0.38-0.84	1200
2013-05-03.35	415.85	75.85	FTN	0.32-1.00	3600
2013-05-04.33	416.83	76.83	FTN	0.32-1.00	3600
2013-05-04.85	417.35	77.35	HCT	0.38-0.68	1800
2013-05-05.08	417.58	77.58	PEN	0.00-0.00	1200
2013-05-09.57	422.07	82.07	FTN	0.32-1.00	3600
2013-05-15.85	428.35	88.35	HCT	0.38-0.84	1200
2013-06-14.64	458.14	118.14	HCT	0.38-0.68	2400
2013-07-13.34	486.84	146.84	FTN	0.32-1.00	3600
2013-08-09.25	513.75	173.75	FTN	0.32-1.00	3600
2013-08-18.25	522.75	182.75	FTN	0.32-1.00	3600
2013-08-19.25	523.75	183.75	FTN	0.32-1.00	3600

^a With reference to the explosion time JD 2456340.0^b For transmission $\geq 50\%$ ^c HCT : HFOSC on 2 m Himalyan Chandra Telescope, India; FTN : FLOYDS on 2 m Faulkes Telescope North, Hawaii; FTS: FLOYDS on 2 m Faulkes Telescope South, Australia; PEN: B&C spectrograph on 1.22 m Galileo Telescope, Italy.